The AAPS Journal (2021) 23: 69
DOI: 10.1208/s12248-021-00598-6

Research Article

Theme: Celebrating Women in the Pharmaceutical Sciences
Guest Editors: Diane Burgess, Marilyn Morris and Meena Subramanyam

Amorphous Solid Dispersions Containing Residual Crystallinity: Competition Between Dissolution and Matrix Crystallization

Dana E. Moseson,[1] Isaac D. Corum,[1] Andres Lust,[1] Kevin J. Altman,[1] Tze Ning Hiew,[1] Ayse Eren,[2] Zoltan K. Nagy,[2] and Lynne S. Taylor[1,3]

Received 17 February 2021; accepted 13 April 2021; published online 17 May 2021

Abstract. Crystallinity in an amorphous solid dispersion (ASD) may negatively impact dissolution performance by causing lost solubility advantage and/or seeding crystal growth leading to desupersaturation. The goal of the study was to evaluate underlying dissolution and crystallization mechanisms resulting from residual crystallinity contained within bicalutamide (BCL)/polyvinylpyrrolidone vinyl acetate copolymer (PVPVA) ASDs produced by hot melt extrusion (HME). In-line Raman spectroscopy, polarized light microscopy, and scanning electron microscopy were used to characterize crystallization kinetics and mechanisms. The fully amorphous ASD (0% crystallinity) did not dissolve completely, and underwent crystallization to the metastable polymorph (form 2), initiating in the amorphous matrix at the interface of the amorphous solid with water. Under non-sink conditions, higher extents of supersaturation were achieved because dissolution initially proceeded unhindered prior to nucleation. ASDs containing residual crystallinity had markedly reduced supersaturation. Solid-mediated crystallization (matrix crystallization) consumed the amorphous solid, growing the stable polymorph (form 1). Under sink conditions, both the fully amorphous ASD and crystalline physical mixture achieve faster release than the ASDs containing residual crystallinity. In the latter systems, matrix crystallization leads to highly agglomerated crystals with high relative surface area. Solution-mediated crystallization was not a significant driver of concentration loss, due to slow crystal growth from solution in the presence of PVPVA. The high risk stemming from residual crystallinity in BCL/PVPVA ASDs stems from (1) fast matrix crystallization propagating from crystal seeds, and (2) growth of the stable crystal form. This study has implications for dissolution performance outcomes of ASDs containing residual crystallinity.

KEY WORDS: amorphous solid dispersion; crystallinity; dissolution,; hot melt extrusion; matrix crystallization.

INTRODUCTION

Amorphous solid dispersions (ASDs), in which an amorphous drug is stabilized by an amorphous polymer as a homogeneous molecular mixture, are an important solubility enhancing platform for poorly water-soluble drugs (1, 2). Dissolution performance is inherently linked to creating and retaining the amorphous form of the drug (3), and extensive research is being conducted to generate a fundamental understanding of release mechanisms from ASDs (4–11). The risk to development of ASD formulations lies in the robustness of the system against crystallization, in both the solid and solution states (12–15).

Pathways of dissolution or crystallization from an ASD formulation are complex (16). Upon contact with aqueous media, the solid can dissolve forming a supersaturated solution or crystallize (matrix crystallization) (17). Solution crystallization, via nucleation and growth pathways, may subsequently occur from the supersaturated solution. Polymers in the ASD can stabilize the amorphous solid during hydration and drug release (18, 19), profoundly impact release mechanisms (11), as well as kinetically stabilize the supersaturated solution (20, 21). The detrimental impact of

Guest Editors: Diane Burgess, Marilyn Morris and Meena Subramanyam

[1] Department of Industrial and Physical Pharmacy, College of Pharmacy, Purdue University, West Lafayette, Indiana 47907, USA.
[2] Charles B. Davidson School of Chemical Engineering, College of Engineering, Purdue University, West Lafayette, Indiana 47907, USA.
[3] To whom correspondence should be addressed. (e–mail: lstaylor@purdue.edu)

matrix crystallization in an *in vitro* or *in vivo* dissolution context is similar to physical stability consideration for amorphous formulations (22, 23). If the amorphous state is not retained, the solubility advantage cannot be realized (24, 25). However, there is little mechanistic understanding of matrix crystallization in ASDs, and most evidence for its occurrence stems from imaging or Raman spectroscopy of crystals developed in or at the surface of an amorphous structure (18, 19, 26, 27).

Dissolution testing during development of amorphous solid dispersion products should be sensitive to variations during product manufacturing or storage that may negatively affect release performance (28, 29). Historically, sink conditions were established because the solubility of active pharmaceutical ingredients (APIs) was typically of little concern both *in vitro* and *in vivo* (30). However, with complex formulations such as ASDs, traditional sink conditions have little relevance to the biopharmaceutical performance (23, 31). Non-sink conditions are essential for evaluating the performance of supersaturating systems, to enable characterization of both dissolution and crystallization kinetics (17, 23, 32, 33). A recent series of studies on tacrolimus brand and generic commercial formulations highlights the relevance of non-sink dissolution testing (34–37). Formulation differences were detected upon accelerated storage (i.e., crystallization occurred), and non-sink conditions were essential for detecting this variation as well as predicting *in vivo* performance.

Dissolution testing has been found to be more sensitive to the presence of crystals or other phase behavior changes in amorphous formulations than most other analytical techniques (38, 39). A recent study by Hermans *et al*. modulated sink/non-sink conditions in an effort to quantitatively detect crystallinity (40). The study found that non-sink conditions could discriminate the level of crystallinity (on a weight basis) of 60-μm particle size bulk crystals added to the dissolution medium (assuming an absence of crystal growth). However, their method under-predicted crystalline content when 2-μm particle size jet milled seeds were used, as they were hypothesized to rapidly dissolve in the media. Greco and Bogner prepared amorphous indomethacin by multiple manufacturing routes, and found that dissolution testing could distinguish differences in the amorphous solids that other techniques could not (41). Li *et al*. reported reduced dissolution rates from spray-dried ritonavir ASDs where phase separation had been induced by the presence of low levels of water in the spray solvent (42).

Crystallinity within an ASD is considered highly detrimental to performance, as it can seed additional crystallization upon storage or upon dissolution (23, 40, 43). A recent review by Ricarte *et al*. highlighted that little is known about the relationship between the solid-state ASD nano-structure and resulting dissolution performance, and in particular identifying acceptable thresholds of crystallinity (44). Several studies by our research group and others have begun to address this knowledge gap, highlighting that the properties of the crystal seeds and the ASD system drive the dissolution performance by a variety of mechanisms. Que *et al.* demonstrated that different external crystal seeds, having altered properties in terms of aspect ratio and relative surface area of fast-growing crystal faces, led to significant differences in desupersaturation rates (45). Purohit *et al.* found that a maximally crystallized ASD had a higher *in vivo* area under the curve (AUC) than the reference crystalline material, suggesting that the crystals formed within the ASD are highly defective (36). In contrast, Wilson *et al*. found that a crystallized ASD had a lower *in vivo* AUC than the reference crystalline suspension (15). Moseson *et al*. demonstrated that a highly effective polymer could prevent growth of residual seed crystals from a HME ASD under non-sink dissolution conditions, ultimately limiting lost solubility advantage; further, residual crystals were more potent than bulk crystals to crystal growth suggesting smaller overall particle size (on a mass basis) and/or highly defective intrinsic structure (24). Hate *et al*. found that the presence of an absorptive sink reduced the overall driving force for crystallization, ultimately lessening the impact of seed crystals on dissolution and absorption (37). Ojo *et al*. found that a non-erodable insoluble carrier entrapped residual crystals, resulting in a diminished impact consuming supersaturation compared to externally added crystal seeds (46).

In this study, release mechanisms and crystallization pathways were evaluated for ASDs of bicalutamide (BCL) and polyvinylpyrrolidone vinyl acetate copolymer (PVPVA) prepared using hot melt extrusion (HME). Hot melt extrusion conditions, if not sufficiently robust, can lead to incomplete amorphization of the input crystalline API (47, 48). Herein, the HME process was varied through the use of different input particle size of crystalline drug and processing temperature, yielding batches containing different levels of residual crystallinity. Five comparative analytical methods were utilized to determine the level of crystallinity within the HME ASDs produced. Dissolution performance of the HME ASDs was evaluated under different dose concentrations, enabling an assessment of release mechanisms with respect to the presence of crystallinity in the ASD or external seeding. The crystallization pathways, polymorphic transitions, and kinetics were monitored with polarized light microscopy (PLM) and Raman spectroscopy.

MATERIALS AND METHODS

Materials

Bicalutamide (BCL) was obtained from ChemShuttle (Hayward, CA). Polyvinylpyrrolidone/vinyl acetate copolymer (PVPVA, Kollidon VA64) was a gift from BASF (Florham Park, NJ). Hydroxypropyl methylcellulose acetate succinate (HPMCAS, Aqoat AS-MF grade) was obtained from Shin-Etsu (Tokyo, Japan). All other materials used were of reagent grade. BCL polymorphs were compared to Cambridge Structural Database refcodes JAYCES01 (form 1) and JAYCES02 (form 2). Several relevant physicochemical properties of BCL and PVPVA are found in Table SI.

Methods

Preparation of Solid-State Forms of BCL

BCL powder was used as-received (“small”), and recrystallized out of ethanol to obtain form 1 crystals of various particle size distribution. Medium-sized crystals (“medium”) were prepared through cooling crystallization out of ethanol using a cooling rate of 10°C/min from 60 to

10°C. Large crystals ("large") were prepared using a direct nucleation control (DNC) cooling crystallization out of ethanol using a cooling rate of 0.1°C/min from 60 to 10°C, and temperature cycling controlled by a focused beam reflectance measurement (FBRM) detector with a particle count threshold of 1500 #/s (49). A ParticleTrack G400 FBRM probe was used to determine the particle count (#/s) using iC FBRMTM Version 4.4.29 software (Mettler Toledo, Columbia, MD). Following each crystallization experiment, crystals were filtered, dried, and sieved to remove agglomerates and achieve a particle size fraction <250 μm for further characterization and ASD preparation. The solid-state form of each API lot was confirmed by X-ray powder diffraction (XRPD) and differential scanning calorimetry (DSC) to be the stable polymorph (form 1) (Figure S1).

Amorphous BCL was prepared by melting crystalline material at 210°C for 10 min on an aluminum weigh boat, then cooling to room temperature. The melt was then cryomilled and sieved to achieve a particle size fraction <250 μm for further characterization. XRPD and DSC characterization are found in Figure S1.

BCL form 2 crystals were prepared from an isothermal hold (100°C for 1 h) of an amorphous BCL melt on an aluminum weigh boat, as described in the literature (50, 51). Seeds were cryomilled and sieved to achieve a particle size fraction <250 μm for further characterization. XRPD and DSC characterization are found in Figure S1.

ASD Preparation by Hot Melt Extrusion

Extrudates were prepared using an Xplore Pharma Melt Extruder (Geleen, The Netherlands), assembled with a 5-mL volume barrel and co-rotating conveying screw (Figure S2a). Four HME ASDs were used for this study prepared from three API lots of varying particle size. The processing strategy aimed to generate ASDs with various levels of residual crystallinity by taking advantage of dissolution kinetics driven primarily by temperature and input crystalline drug particle size. The processing temperature was set to generate a product melt temperature in the dissolution regime, between T_c = 145°C and T_m = 195°C, as guided by the temperature-composition phase diagram for the 30% drug loading composition (Figure S2b), while residence time and screw speed were held constant. A summary of processing conditions is found in Table SII. The small crystals were processed at both 180 and 155°C (formulations S/180 and S/155), while medium and large crystals were processed only at 155°C (formulations M/155 and L/155). Product melt temperature was recorded from a thermocouple located near the extruder die. Residence time was independently controlled through the use of the recirculation loop, and was considered the point when the recirculation valve was opened and the melt began extruding through the die. In all experiments, the total extrusion time ranged from the noted time until approximately 1 min later.

Solid State and Particle Characterization

X-Ray Powder Diffraction. Solid-state form of API, physical mixtures, and ASD samples was confirmed by X-ray powder diffraction (XRPD) analysis using a Rigaku SmartLab diffractometer (Rigaku Americas, The Woodlands, TX) in Bragg-Brentano mode with a Cu-kα radiation source and d/tex ultra detector scanned over the range of 5–40° 2θ with a step size of 0.02° and a 2°/min scan rate.

For crystallinity quantification, a calibration curve covering the 0–65% crystalline content range (R^2 = 0.9952) was generated for the 17.2° 2θ peak area, using a step size of 0.02° and a 0.5°/min scan rate over 16–18° 2θ. Calibration standards were prepared in triplicate by spiking crystalline BCL (small) into a fully amorphous BCL/PVPVA ASD sample through geometric mixing. The raw data (background subtracted) was processed using a moving average filter in order to maximize the signal-to-noise ratio. The LOD and LOQ were found to be approximately 1% and 3% crystalline content respectively based on 3:1 and 10:1 signal-to-noise ratio of peak intensity to the baseline. Extrudate powders were scanned in triplicate to determine the % crystallinity.

Thermal Analysis. Solid-state forms of BCL and ASD samples were evaluated by differential scanning calorimetry (DSC) using a Q2000 DSC equipped with a refrigerated cooling accessory (TA Instruments, New Castle, DE) purged with nitrogen at 50 mL/min. API samples (3–5 mg) were loaded into standard aluminum pans, and a heat-cool-heat method was used with 10°C/min heating and cooling rates. ASD samples (3–5 mg) were heated from 0 to 180°C at 5°C/min with modulation of ±0.796 every minute, then cooled to 0°C at 10°C/min, followed by a second heating ramp at 10°C/min.

Microscopy. ASD particles were loaded in mineral oil on a glass slide and visually observed for birefringence using a Nikon Eclipse E600 POL cross-polarized light microscope (×20 objective) with Nikon DS-Ri2 camera (Melville, NY). At least five images were captured to characterize the sample.

A FEI TeneoVS scanning electron microscope (FEI Company, Hillsboro, OR) with an ETD detector using operating conditions of 5 kV accelerating voltage, 0.10 nA current, and ~10 mm working distance to image platinum-coated samples.

Transmission electron microscopy (TEM) images in bright field and diffraction mode were acquired in an FEI Tecnai G20 electron microscope (FEI, Hillsboro, OR) equipped with a LaB6 source, X-max 80-mm^2 silicon drift detector (Oxford Instruments, Abingdon, Oxfordshire, UK), and operated at 200 keV, 100-μm aperture, and a spot size of 3. By gently touching/wiping the interior of the vial lid, which contained particulates fragmented from the bulk extrudate rods, small extrudate particles were sprinkled on 300 mesh carbon-coated copper TEM grids with 5–6 nm standard thickness (SPI supplies, West Chester, PA). At least three grid squares were analyzed to identify particles that were suitably electron transparent for imaging. Fast Fourier transform (FFT) analysis was performed within Gatan DigitalMicrograph 3.21 software suite (Pleasanton, CA).

Particle Size and Surface Area Analysis. Particle size of API samples was determined in triplicate using a Malvern Mastersizer 3000 particle size analyzer with Aero S attachment (Worcestershire, UK). BET surface area analysis of API samples was performed using a 5-point BET method (ASAP 2020 Plus, Micromeritics, Norcross, GA).

Solubility and Dissolution Studies

Solubility Studies. Apparent solubility studies of the as-received BCL (form 1, small), metastable polymorph (form 2), and amorphous form were conducted. A Hanson Vision G2 Classic 6 dissolution system (Teledyne Hanson Research, Chatsworth, CA) with 150-mL small volume vessels was used, equipped with a Pion Rainbow Dynamic Dissolution Monitor system (Pion Inc., Billerica, MA) with 10-mm path length probes for in-line concentration detection. An excess of each sample (50 mg) was added to 100 mL of 50 mM pH 6.8 phosphate buffer at 37°C stirred at 100 rpm over approximately 20 h and monitored for concentration against a second derivative calibration curve over the 298 to 308 nm range. In separate experiments, PVPVA at 70 μg/mL and HPMCAS at 1 mg/mL were added to the buffer to assess supersaturation potential and kinetics of polymorphic transitions. Experiments were conducted in triplicate.

A fluorescent probe, pyrene, was used to detect the onset of liquid-liquid phase separation, and thus the amorphous solubility of BCL. The emission spectrum of pyrene has been used to detect changes that occur to the polarity of its environment as it partitions into a drug-rich phase formed above the amorphous solubility boundary (16, 52, 53). BCL solutions were prepared by anti-solvent addition from a 10 mg/mL BCL stock solution in dimethyl sulfoxide (DMSO) into the buffer system held at 37°C, with and without polymeric additives, and containing 1 μg/mL pyrene. Solutions were excited at 322 nm, and emission spectra were collected from 350 to 600 nm using a Shimadzu RF-5301 PC spectrofluorometer (Kyoto, Japan) and slit widths 5 and 1.5 nm. Solutions in buffer alone were measured within 1 min of preparation, while solutions containing polymeric additives were measured within 5 min of preparation. The ratio of peak intensity of the first and third emission peak (I_1/I_3) was used to assess changes to the environment of pyrene.

A Pion Rainbow Dynamic Dissolution Monitor system with 5-mm path length probes was used to develop a concentration *vs.* absorbance relationship to determine the amorphous solubility in the presence of polymeric additives based on anti-solvent addition from a 10 mg/mL BCL stock solution in dimethyl sulfoxide (DMSO) into the buffer system held at 37°C. The experiment could not be conducted in the absence of polymers due to the rapid crystallization of BCL at high supersaturation. Three UV criteria were used: (1) absorbance at 304 nm, (2) extinction at 450 nm (light scattering), and (3) second derivative absorbance area under the curve (AUC) between 298 and 308 nm. The formation of a drug-rich phase results in light scattering and changes to the UV extinction coefficient and curve shape, which can be used to indicate the onset of liquid-liquid phase separation, and thus the amorphous solubility boundary (16).

Nanoparticle tracking analysis (NTA) and dynamic light scattering (DLS) methods were used to detect the presence of nanodroplets above the amorphous solubility boundary. BCL solutions of 0–200 μg/mL concentration were prepared by anti-solvent addition, as above, into buffer held at 37°C containing 70 μg/mL PVPVA. DLS analysis was performed using a Zetasizer Nano ZS (Malvern Instruments, Westborough, MA), and NTA was performed with a NanoSight LM10 (Malvern Instruments, Westborough, MA).

Nucleation and Crystal Growth. Supersaturated solutions of BCL were generated by anti-solvent addition, as above, into 100 mL of buffer with and without polymeric additives held at 37°C, while being stirred at 100 rpm. Nucleation induction time was taken as the time at which the concentration decreased by 1%. For crystal growth measurements, crystal seeds of BCL form 1 (small) were added to supersaturated solutions with and without polymeric additives and monitored for changes in concentration over time while being stirred at 100 rpm. Solutions were monitored for the desupersaturation rate while being stirred at 100 rpm. Experiments were conducted in triplicate.

Dissolution Studies. The dissolution study design (Table SIII) utilized several levels of sink/non-sink conditions with respect to the crystalline and amorphous solubility of BCL. Dissolution experiments were monitored for 4 h. Variations of the dissolution experiment were conducted to evaluate the effect of external seeding (by adding crystal seeds equivalent to 10% of the BCL dose) and 1 mg/mL HPMCAS pre-dissolved in the dissolution buffer. Experiments were conducted in triplicate.

Precipitates from several experiments conducted at 150 μg/mL theoretical maximum BCL concentration were filtered, and XRPD patterns were collected to identify the crystalline form(s) present using the method parameters described above.

Polymer Release Characterization. The release of PVPVA from selected ASDs over 1 h was quantified using the experimental setup described above using the 30 μg/mL BCL dose condition. At each pre-determined time point, 2 mL of dissolution medium was withdrawn and replenished with an equal volume of fresh medium. Prior to quantification, the aliquots were filtered through a 13-mm diameter 0.45-μm PTFE syringe filter (Basix, Fisher Scientific, Pittsburg, PA).

The concentration of PVPVA was quantified by size exclusion chromatography on a 1260 Infinity II high-performance liquid chromatography system (Agilent Technologies, Santa Clara, CA). The chromatographic analysis was performed at 40°C with an A2500, aqueous GPC/SEC column (6-μm particle size, 8 mm × 300 mm, molecular weight exclusion limit of 10000 Da for pullulan, Malvern Panalytical, Worcestershire, UK) as the stationary phase. The mobile phase comprised of 80% purified water and 20% methanol, v/v eluted at a flow rate of 0.5 mL/min. The injection volume used was 10 μL. The peak corresponding to PVPVA has a retention time of 10.2 min and was detected using an ultraviolet detector at a wavelength of 205 nm. A standard curve built with a linear regression model for the concentration range of 5–100 μg/mL yielded an R^2 value of 0.999.

Crystallization Studies

Polarized Light Microscopy. ASD particles were immersed in dissolution buffer on a glass slide heated to 37°C on a hot stage to observe the progression of crystallization.

Images were periodically captured using a Nikon Eclipse E600 POL cross-polarized light microscope (×20 objective) with Nikon DS-Ri2 camera.

Raman Spectroscopy. Raman spectroscopy was performed using a Kaiser RXN2 Hybrid Raman analyzer (Kaiser Optical Systems, Ann Arbor, MI) equipped with 785-nm laser. The spectra of solid samples were collected with a P^hAT system probe head (nominal focal length 250 mm, nominal beam diameter at focal position 6 mm, focal tolerance ±12 mm) and CCD detector operating at −40°C. The laser power was set at 100 mW. The detection region ranged from 1800 to 300 cm^{-1} and a 5-s integration time was used. The spectral region from 1800 to 900 $cm^{-1}$was used for further analysis.

In order to determine the crystallization onset time and also a kinetic profile, a slurry test was performed. In brief, suspensions of 10 mg/mL BCL were generated using 400 mg of ASD powder in 12 mL dissolution buffer kept at 37°C and stirred at 200 rpm using an X-shaped stir bar. The powder was initially suspended in dissolution buffer using a vortex mixer for 5 s. *In situ* Raman spectroscopy of slurries was performed using a Raman Rxn probe equipped with a 152.4-mm-long MR immersion optic with 6.35-mm outer diameter. The power was set at 400 mW and a 30-s integration time was used. Sampling was done every 2 min for up to 2 h, with the first measurement taken at 1 min. Precipitates from select Raman experiments were filtered and XRPD patterns were collected to identify the crystalline form(s) present using the method parameters described above. SEM images of representative precipitates were collected as described above.

Multivariate curve resolution alternating least squares (MCR-ALS) was used for modeling the Raman scattering data collected during slurry testing. MCR-ALS was performed with Unscrambler X® (Version 10.3, Camo software, Oslo, Norway). The Raman spectra were pre-processed using standard normal variate (SNV) correction and the data range from 1551 to 1166 cm^{-1} was used for analysis. Closure and non-negative concentrations were used as constraints during modeling and the maximum number of ALS iterations was set at 100. The sensitivity to pure components was set at the lowest value. Spectra of pure solid-state forms suspended in buffers were used for initial guess.

Relative crystal growth rates were calculated for each replicate from the linear portion of the component concentration curve. Paired, one-tailed Student's *t* test were performed in Microsoft Excel.

RESULTS

API Characterization

Solubility

Bicalutamide (BCL) is a Biopharmaceutics Classification System (BCS) class 2 drug, with low aqueous solubility. It has two known polymorphic forms: thermodynamically stable form 1 and metastable form 2 (50, 51), with apparent solubility measured at 4.3 and 15 μg/mL, respectively (Figure S3–S4). When converted to the amorphous form, its apparent solubility increases to 150 μg/mL (Figures S5–S9). This translates to a maximum solubility advantage of 35 times over the crystalline solubility of the stable polymorph (form 1), if the amorphous solid can dissolve to its miscibility limit with water without triggering nucleation or crystal growth events.

Nucleation and Crystal Growth from Supersaturated Solutions

In supersaturated solutions, BCL nucleates in under 30 min in the absence of polymer in the buffer (Fig. S10a). At the highest supersaturation condition, in the absence of polymeric additives, nucleation takes place in under 5 min, confirming that BCL is a fast crystallizing compound in a solution environment. HPMCAS was found to be more effective as a nucleation and crystal growth inhibitor, in comparison to PVPVA. Nucleation time in the presence of PVPVA at 70 μg/mL reduces as supersaturation increases, but remains above 1 h even at the highest solution concentration measured. In the presence of HPMCAS at 1 mg/mL at all supersaturation conditions, nucleation is inhibited for the monitoring period (8 h). This indicates that a solution-mediated nucleation event is not expected to occur during the timeframe of the dissolution experiments, as all achieved concentrations remained below ~40 μg/mL, regardless of the dose used.

As shown in Fig. S10b, crystal growth of form 1 crystals was measured in supersaturated solutions of BCL (30 and 150 μg/mL) by monitoring the initial desupersaturation curve. In lower supersaturation conditions (30 μg/mL BCL concentration), the crystal growth of BCL form 1 crystal seeds was near zero, indicating that BCL has slow solution-mediated crystal growth behavior at this supersaturation condition, which was not affected by polymeric additives in the media. However, at high supersaturation (150 μg/mL BCL), crystal growth was extremely rapid. By including polymeric additives, the growth rate was reduced. The effectiveness (E_G) of the polymer at inhibiting the crystal growth of the BCL seeds can be expressed using the following equation (Eq. 1)

$$E_G = \frac{R_{G,np}}{R_{G,p}} \tag{1}$$

where $R_{G,np}$ and $R_{G,p}$ are the crystal growth rates in the absence and presence of polymer (54). A value of $E_G > 1$ indicates that the polymer is effective at disrupting growth. Although the polymer effectiveness ratio (E_G) was found to be 8.6 for 70 μg/mL PVPVA, indicating that while PVPVA is a moderately effective crystal growth inhibitor of BCL, crystal growth remains at a rapid, yet reduced rate. Growth is brought to a near zero rate when 1 mg/mL HPMCAS is included in the buffer (E_G = 158), indicating that HPMCAS is a highly effective solution-mediated crystal growth inhibitor of BCL.

ASD Processing and Characterization

Formulation and Processing of HME Samples

In order to improve dissolution characteristics, BCL was formulated as an ASD with PVPVA. PVPVA was selected due

to its prevalence in HME formulations, favorable processing characteristics, and dissolution rate enhancement potential (1, 26, 55–58). Flory-Huggins modeling of the temperature-composition phase diagram generated an interaction parameter of $\chi = -1.57$, which indicates favorable miscibility of the system (Figure S2b) (47). The system was anticipated to have acceptable physical stability characteristics, due to the miscibility of the drug-polymer system, and stability evidence found in the literature of high drug loading ASDs of BCL and the chemically related polymer PVP (59, 60).

Process variation was induced by modifying the processing temperature (Table SII) and using input crystalline material of various particle sizes (Fig. S11-S12). Use of different particle size represents extremes of real-world variation on input material, and allows for examination of process robustness against such variations. BCL crystals as-received (small) present as a highly cohesive micronized powder, with a D_{50} particle size = 3.5 μm. Upon recrystallization, 10-fold and 26-fold increases in D_{50} particle size were achieved (38 μm: medium; and 93 μm: large). This increase in particle size reflects a 12- and 7-fold reduction in specific surface area (SSA).

Characterization of HME Samples for Crystallinity

Several techniques were employed to characterize the presence or absence of crystallinity in each of the four batches, as each analytical tool has limitations which lead to different descriptions of amorphous or crystalline character (Table I) (47, 61–64). The least sensitive technique employed to assess crystallinity was DSC. A T_g (inflection) is identified for each sample at approximately 98°C (Fig. 1a), confirming the formation of an ASD by HME processing. Because of the miscibility of the drug-polymer system, rather than detecting a clear crystalline melting peak in samples with some crystallinity, a dissolution endotherm, corresponding to the dissolution of crystals into the polymer melt, can sometimes be observed (47). For the other formulations, no clear dissolution endotherm can be detected. In the non-reversing heat flow, this shallow and broad endothermic shift in the baseline can be seen in the L/155 sample over the temperature range of 120–170°C, providing a positive, albeit insensitive identification of crystalline content.

XRPD is the standard technique for crystallinity quantification, but is limited by excipient dilution, crystal quality, and method parameters (47, 62, 63). Two sets of method parameters were used to characterize the four ASD samples: range 5–40° 2θ at 2°/min, and 16–18° 2θ at 0.5°/min. Characteristic crystalline peaks were observed only in the sample with highest level of crystallinity, L/155, when scanning at the faster speed (Fig. 1b). By scanning over a narrower range with a slower rate 0.5°/min, crystallinity could be quantified for two of the samples, M/155 (3.5%) and L/155 (30%).

PLM is a highly sensitive, but non-quantitative, method used to detect crystallinity (47, 64, 65). Here, crystals are observed in the M/155 and L/155 samples only (Fig. 1c). However, strain birefringence was also observed, which makes birefringence alone a somewhat equivocal property. In the PLM images, residual crystals appear with a brighter white birefringence (indicated by white arrows), while the strain birefringence appears as hazy orange or blue (indicated by yellow arrows).

Scanning electron microscopy (SEM) is often considered highly sensitive to detect low levels of crystal growth on ASD particle surfaces. However, detectability is limited in these samples because crystals are not located primarily at surfaces. As shown in Fig. 1d, smooth particle topography is observed in S/180, S/155, and M/155 ASDs (0–3.5% residual crystallinity). In contrast, the particle surface of L/155 ASD (30% residual crystallinity) is rough due to the large quantity of embedded crystals which measure 340 ± 140 nm in length ($n = 30$).

Lastly, transmission electron microscopy (TEM) was used to provide a high-resolution identification of crystalline content, due to its ability to identify and spatially differentiate crystalline and amorphous regions (64). The TEM images found in Fig. 1e identify S/180 as fully amorphous through several indicators. First, the diffraction pattern of the particle does not have diffraction spots which would indicate crystallinity. Additionally, its generally homogeneous, continuous appearance indicates that the particle is of similar thickness throughout and does not have regions which induce electron scattering (such as crystalline domains), which would appear darker. The three other HME ASDs (S/155, M/155, and L/155) have greater heterogeneity in particulate structure, due to embedded crystallites, as well as variation in particle thickness. In each, multiple, randomly oriented crystallites contribute to forming the diffraction pattern. Since crystallinity was observed in S/155 by TEM, but not by the quantitative XRPD method, it is considered to have <1% crystallinity. As crystallinity was not observed by TEM in S/180, it is considered to be fully amorphous (0% crystallinity).

An electron transparent extrudate particle from S/155 ASD is shown in Fig. S13, which has residual crystals clearly identifiable based on their dark coloration and diffraction contrast. The residual crystals in this extrudate particle are 140 ± 10 nm ($n = 10$). This nanometer size range is consistent with the size of residual crystals observed in HME extrudates (24, 64, 66), and follows from the general size reduction expected via a crystal dissolution pathway (47, 64, 67). Additionally, the uniform size is consistent with the narrow particle size distribution starting material of the as-received (small crystals) lot, which had a D_{10}–D_{90} range of 1.3–8.6 μm.

Table I. Crystallinity Characterization Summary of BCL:PVPVA HME ASDs

Sample ID	% crystallinity by XRPD	Crystallinity observed by DSC	Crystallinity observed by SEM	Crystallinity observed by PLM	Crystallinity observed by TEM
S/180	<LOD (0%)	No	No	No	No
S/155	<LOD (<1%)	No	No	No	Yes
M/155	3.5%	No	No	Yes	Yes
L/155	30%	Yes	Yes	Yes	Yes

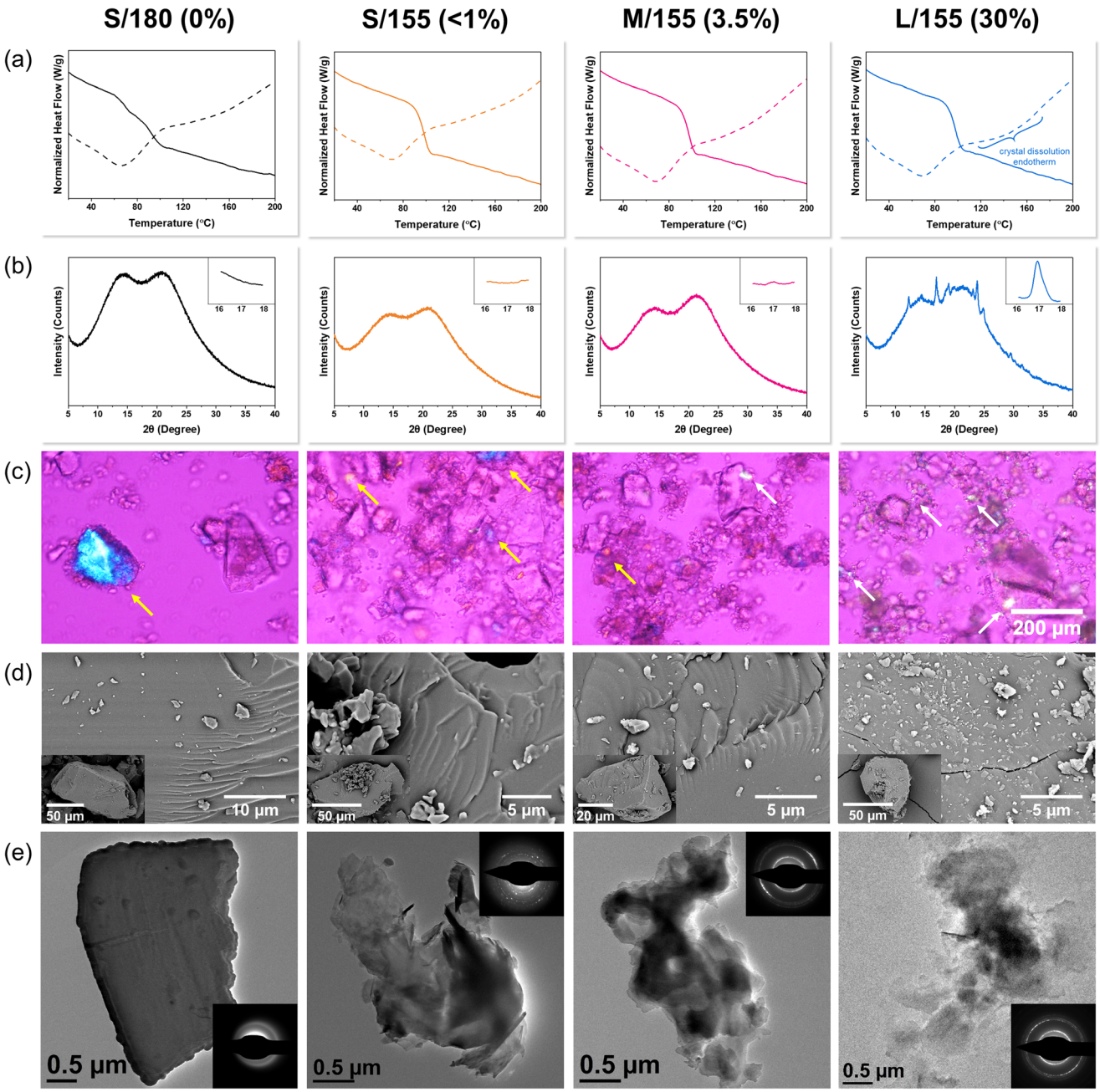

Fig. 1. Solid state and microscopy characterization of HME ASD samples S/180 (0% crystallinity), S/155 (<1% crystallinity), M/155 (3.5% crystallinity), and L/155 (30% crystallinity). **a** Modulated DSC traces of HME ASD samples: reversing (solid line) and non-reversing heat flow (dashed line). The presence of crystallinity is observable in the non-reversing heat flow curve of the L/155 sample. **b** XRPD patterns of HME ASD samples at scan rates of 2°/min over 5–40° 2θ and (inset) 0.5°/min over 16–18° 2θ. The 0.5°/min scan rate was used to quantify the level of crystallinity in the samples. **c** PLM images of HME particles. Strain birefringence is highlighted by the yellow arrows, while residual crystals are highlighted by white arrows. **d** Backscatter SEM images of HME particles. Embedded residual crystals are apparent in the L/155 ASD sample. **e** Representative bright field TEM micrographs and corresponding diffraction patterns (inset) of HME ASD extrudate particulates

Dissolution and Crystallization Behavior

BCL Release Studies

Non-sink Conditions. The dissolution behavior of four HME ASDs containing 0–30% crystallinity was assessed under sink and non-sink conditions so as to enable an assessment of impact of crystallinity on supersaturation profiles, as well as uncover crystallization mechanisms (Fig. 2). At the 30 μg/mL dose (Fig. 2c), the S/180 ASD (0% crystallinity) achieves ~18 μg/mL with little desupersaturation observed, which indicates that crystallization occurred in the dissolving solid preventing complete release of the amorphous content. Similarly, at the 60 μg/mL and 150 μg/mL doses (Fig. 2a, b), the S/180 ASD achieves a maximum

concentration of ~40 μg/mL in about 1.5–2 h, followed by slow desupersaturation. This suggests that the larger dose did not contribute to generating a greater level of supersaturation, before crystallization rates exceeded dissolution rates. Both form 1 and form 2 polymorphs were observed by XRPD (Fig. S14) in the solids recovered after ~20 h of continued mixing, consistent with the apparent solubility experiments (Fig. S4) in which both polymorphs were present following dissolution/crystallization of amorphous BCL in the presence of PVPVA. As minimal desupersaturation is observed except under the highest dose condition, this suggests that the solid-mediated (matrix) crystallization pathway dominates across the range of dose conditions, while solution-mediated crystallization requires high supersaturation to be achieved.

The HME ASDs containing residual crystallinity achieve lower supersaturation levels than the fully amorphous S/180 ASD at all non-sink dose conditions (30–150 μg/mL). In the 30- and 60-μg/mL dose conditions (Fig. 2b, c), the three HME ASDs containing residual crystallinity quickly reach their plateau concentrations in 15–60 min, a shorter timeframe than the crystal-free ASD S/180. The crystalline physical mixture (100% crystallinity) reaches its solubility value, ~4.3 μg/mL. Solid-mediated crystal growth (i.e., crystallization within the ASD matrix) is thus suggested as the dominant crystallization pathway, due to the lack of extensive desupersaturation, which would otherwise indicate solution-mediated crystal growth.

At the 150-μg/mL dose conditions, the S/155 ASD (<1% crystallinity) followed a similar dissolution curve as S/180 for the first 45 min reaching ~32 μg/mL, but then began desupersaturating as the crystal growth rate outpaced the dissolution rate (Fig. 2a). Similarly, the M/155 ASD (3.5% crystallinity) had fast initial dissolution for 30 min reaching ~28 μg/mL, then began desupersaturating. For these two formulations, the high level of amorphous material available for dissolution (compared with the initial level of residual crystallinity) dominates the kinetics at early timepoints. Eventually, the residual crystallinity has grown extensively through the matrix to generate high crystalline surface area, which then enables solution-mediated crystal growth to outpace dissolution rates. The L/155 ASD (30% crystallinity) quickly reached a plateau concentration in under 30 min of ~10 μg/mL, and little desupersaturation was observed. Because the mass fraction of crystallinity is so much greater than the S/155 and M/155 ASDs, the solid-mediated crystal growth dominated the dissolution profile, and little supersaturation was achieved. In contrast to S/180 ASD, only form 1 was observed by XRPD for the HME ASDs which contained residual crystals of form 1.

The dissolution/crystallization pathways were further investigated by use of external seeding by adding 10% small

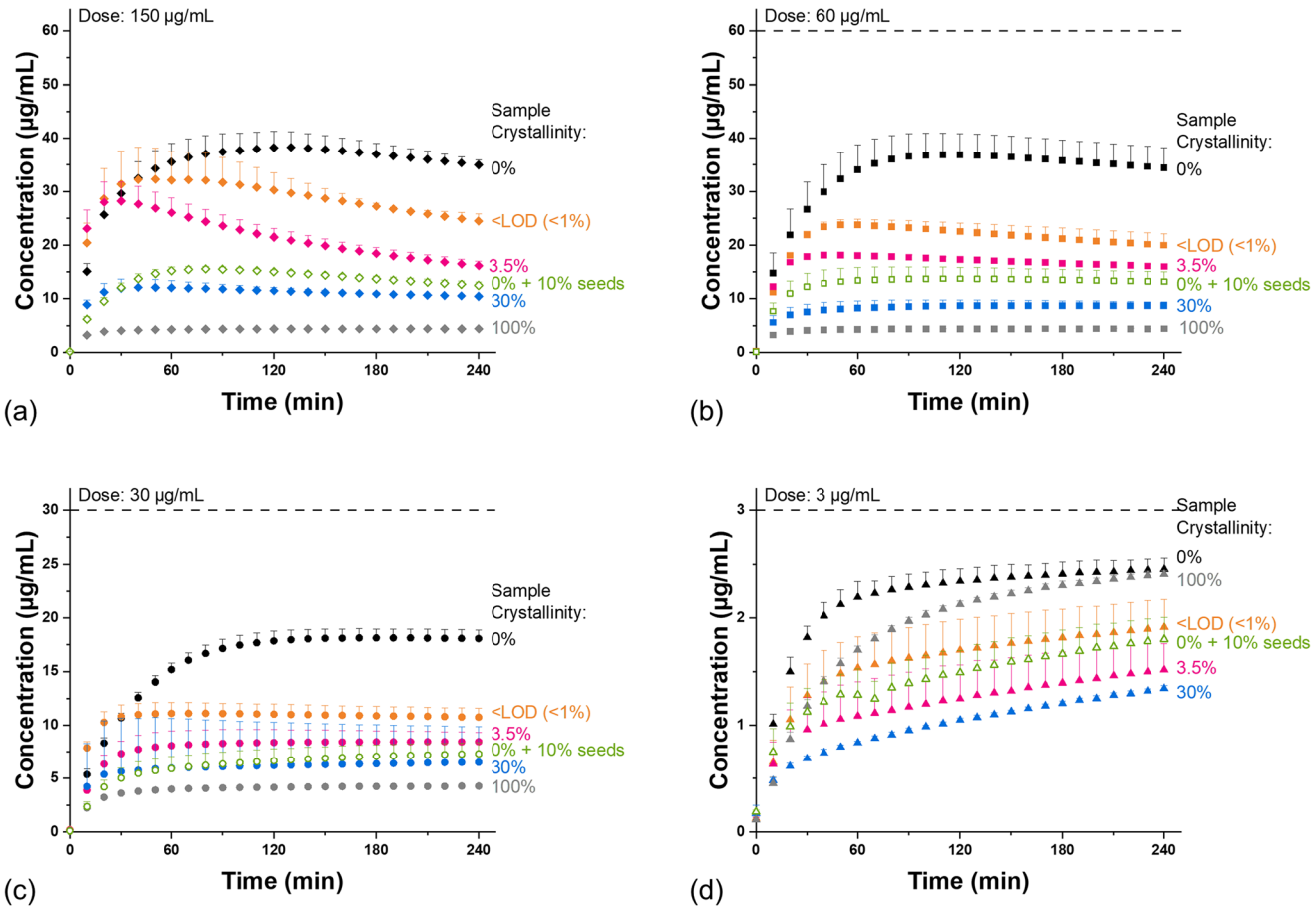

Fig. 2. Dissolution of HME ASDs (0, <1%, and 3.5%, 30% crystallinity), physical mixture (100% crystallinity), and S/180 ASD (0% crystallinity) with 10% external crystal seeds added under non-sink and sink conditions: **a** 150 μg/mL, **b** 60 μg/mL, and **c** 30 μg/mL, and **d** 3 μg/mL. Error bar indicates one standard deviation (n=3), and is too small to be seen in some samples

crystals (form 1) to the dose of HME ASD S/180. Under each non-sink dose condition, these samples reached plateau concentrations in the range of the HME ASDs with similar levels of residual crystals. Since a high degree of supersaturation was not achieved at any dose condition, this suggests that the crystalline material, regardless of its origin or initial location with respect to the amorphous solid, grew rapidly through solid-mediated crystallization based on association with the amorphous solid in the media.

Sink Conditions. Sink conditions were explored using a dose concentration of 3 μg/mL (Fig. 2d). While this value does not meet the traditional definition of sink conditions, it was the lowest value that could practically be explored due to weighing constraints and without including solubilizing additives in the dissolution media. The S/180 ASD achieved a fast dissolution rate and a maximum dissolved concentration of 2.8 μg/mL in the 4-h monitoring period. The crystalline physical mixture (small crystals) similarly achieved this value at a slightly slower rate than the S/180 ASD, consistent with dissolution rate differences influenced by solubility of the BCL solid-state form. Interestingly, each of the HME ASDs which contained residual crystallinity had markedly slower dissolution rates and did not reach the same final dissolution extent as the fully amorphous ASD and crystalline physical mixture during the experiment timeframe (4 h). This can be explained by the presence of locally high supersaturation in the amorphous solid surrounding the residual crystals. The crystals experience rapid crystal growth, consuming the amorphous solid, and create relatively large and/or agglomerated crystals. This low relative surface area of the newly grown crystals results in a slower dissolution rate than found even from the crystalline physical mixture, which has high relative surface area due to the small particle size. The externally seeded sample had a similar trend, indicating that the seeds, despite not being present within the ASD matrix, associated with the amorphous solid and induced crystallization.

Crystallization Observations by PLM

PLM imaging of the particles exposed to dissolution media indicates that crystals are growing through solid-state matrix crystallization within the ASD particles (Fig. 3). Crystals appear at interfaces of the crystal-free ASD solid (S/180) and dissolution media around 10–20 min (Fig. 3a). After 60 min, some amorphous solid remains with more crystals observable at interfaces and throughout the solid. With the S/155 ASD (<1% crystallinity), crystals first appear embedded within the amorphous solid after ~20 min, once they have grown to a sufficient size (Fig. 3b). After 60 min, no amorphous solid is apparent, having been consumed by the crystals which originated from within the solid. Crystals are easily observed in the L/155 ASD (30% crystallinity) at the initial time point (Fig. 3c). Within 20 min, all solid appears to have been converted to crystalline material. Clearly, the presence and level of residual crystals alters the kinetics of the solid-state amorphous-to-crystalline transformation within the amorphous solid. The crystallization of the S/180 ASD was also observed in the presence of crystal seeds (Fig. 3d). The crystal seeds are dispersed within the media, and some appear in proximity to the ASD solid. These crystals quickly consume the amorphous solid.

Crystallization Observations by In-Line Raman Spectroscopy

Crystallization Kinetics of Fully Amorphous ASD. The MCR-ALS modeling of Raman spectra enabled analysis of crystallization outcomes and kinetics of different BCL ASDs in the presence of dissolution medium (Fig. 4). Consistent with the visual observations by PLM (Fig. 3a), the S/180 ASD begins crystallizing in 20–30 min, and completely crystallizes within approximately 1 h, transforming from component 1 (consistent with the BCL/PVPVA ASD) to component 2 (consistent with crystalline BCL polymorph form 2). (Refer to Figs. S16 and S17 for comparison of component spectra and standards used for MCR-ALS modeling.)

Crystallization mechanisms were probed by including 1 mg/mL HPMCAS in the dissolution medium, as this additive was found to be an excellent inhibitor of nucleation and solution-mediated crystal growth (Fig. S10). Nucleation (as inferred from the lag time) was delayed by approximately 10 min. This again confirms the dominance of the matrix crystallization route, since crystallization occurred irrespective of the presence of the polymeric additive. In both cases, with and without the HPMCAS additive, the metastable polymorph (form 2) is formed based on MCR-ALS modeling and confirmed by XRPD (Fig. S15). No significant change in crystal growth rate of form 2 was observed as a result of inclusion of HPMCAS in the buffer.

Crystallization Kinetics of ASDs Containing Residual Crystallinity or External Seeds. The crystallization kinetics of two ASD samples containing residual crystallinity were also evaluated using in-line Raman spectroscopy and MCR-ALS (Fig. 4). All component and standard spectra used for MCR-ALS modeling are found in Fig. S17. The S/155 ASD (<1% crystallinity) grows only form 1 crystals during the experiment, transitioning from component 1 (consistent with the BCL/PVPVA ASD) to component 3 (consistent with crystalline BCL polymorph form 1). Crystalline BCL form 1 first appears at a detectable level at approximately 15 min, and completely crystallizes within 1 h. By including HPMCAS in the buffer, the overall growth rate of form 1 crystals in this sample decreases. The M/155 ASD (3.5% crystallinity) crystallizes faster than the S/155 ASD, both in the first appearance of a detectable level (7 min), and in the overall growth rate. This indicates that the M/155 has greater overall crystal surface area, consistent with the greater level of crystals measured in the formulation.

By including 10% external seeds of form 1 along with the crystal-free ASD, comparisons to the ASDs with residual crystals can be made. Because of greater crystal mass, there was no lag time required for the form 1 crystals to grow to a detectable level. Interestingly, the overall growth rate of these crystals was slower than that measured for both S/155 and M/155 ASDs (Fig. 4), indicating that despite the greater quantity

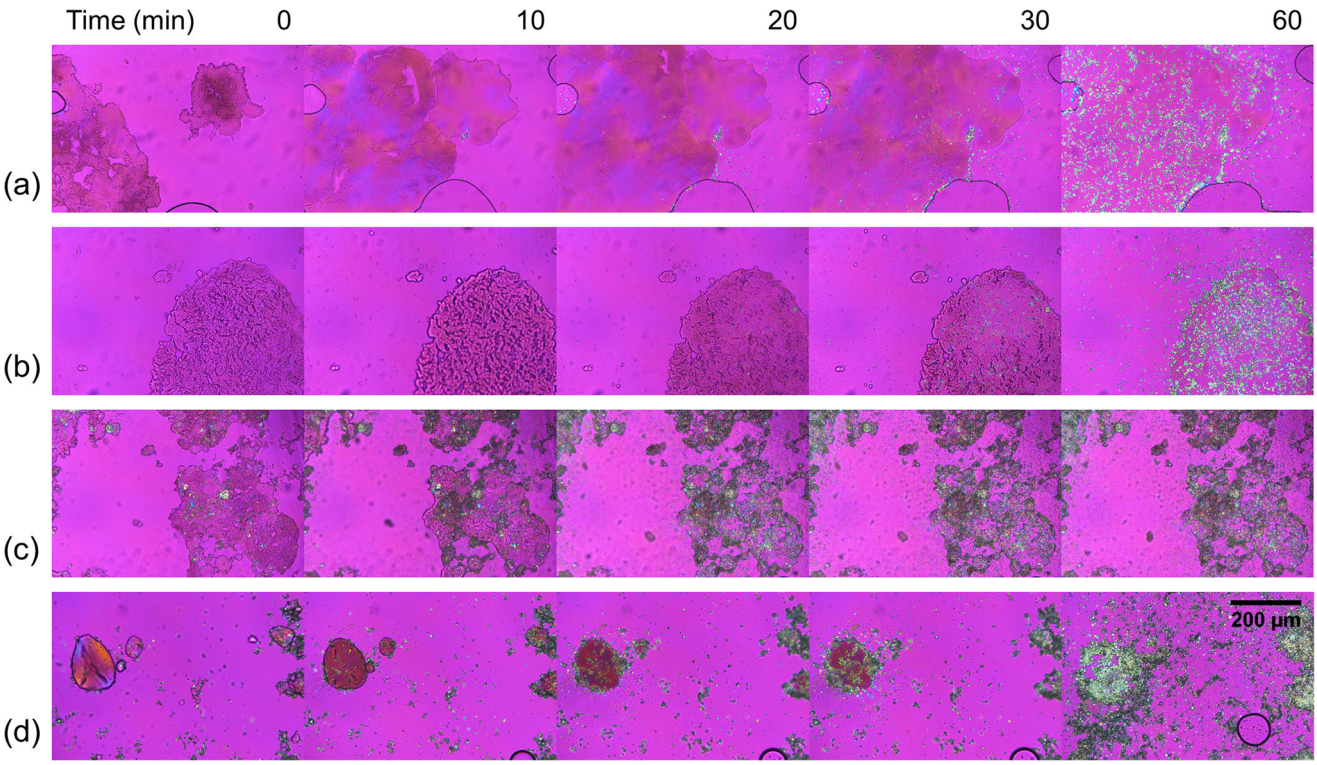

Fig. 3. Time lapse polarized light micrographs of BCL/PVPVA dissolving into buffer held at 37°C: **a** S/180 ASD (0% crystallinity), **b** S/155 ASD (<1% crystallinity), **c** L/155 ASD (30% crystallinity), and **d** S/180 ASD (0% crystallinity) with externally added seeds

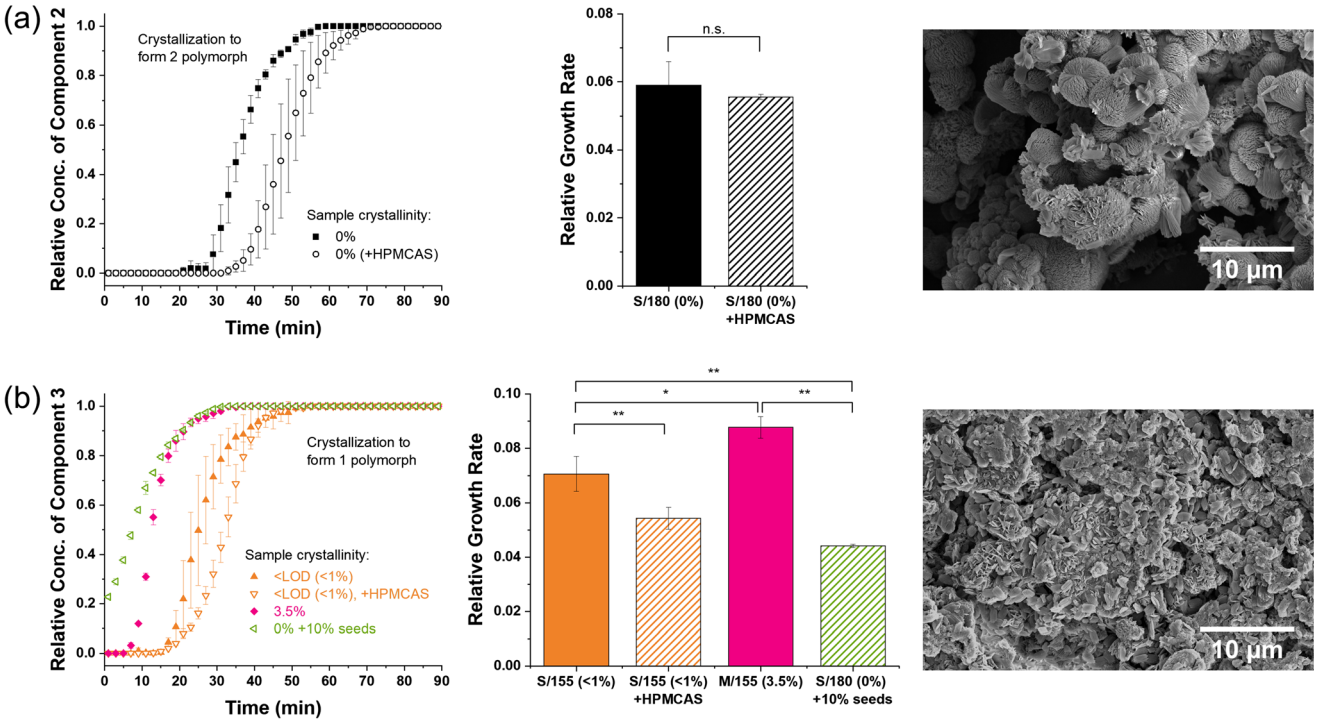

Fig. 4. Crystallization kinetics of ASD samples **a** without and **b** with crystalline content, and representative SEM images of solids harvested after 2 h of dissolution. The *t* test *p*-values are as follows: not significant (n.s.), <0.05 (*), and *p*-value <0.01 (**). Error bar indicates one standard deviation (n=3), and is too small to be seen in some samples

(10% compared to 0–3.5% crystals), the external seed crystals have overall lower surface area available for crystal growth.

Microstructural Progression of ASD Particles During Dissolution

SEM images of the ASD particle surface after 20 min of exposure to buffer show a rough and pitted structure (Fig. S18). Similar surface structures have been observed by Saboo *et al*. for incongruently releasing ASDs (10, 11, 26), in which a drug-rich layer is left behind following preferential polymer release. In the sample with residual crystallinity (Fig. S18b), the surface has two distinct topographical regions indicating some areas have begun to crystallize, while some surface areas remain amorphous (and presumably drug-rich given the porous appearance).

Following the completion of dissolution experiments, the ASD systems have completely crystallized (Fig. 4). The formation of different polymorphs from ASD systems with and without residual crystals is supported by SEM morphology of harvested solid material. As seen in Fig. 4a, harvested solid identified as polymorph form 2 by Raman spectroscopy and XRPD (Fig. 4a and Fig. S15) has a needle-shaped morphology where the needles grow in circular clusters. In contrast, harvested solid (Fig. 4b) identified as polymorph form 1 by Raman spectroscopy and XRPD (Fig. 4b and Fig. S15), has an irregular plate-shaped morphology. While this morphology does not match that of the original crystals (Fig. S12), changes in crystal habit and growth patterns are observed when grown under different supersaturation conditions or in the presence of additives (68–70).

Polymer Release Behavior

The dissolution behavior of PVPVA from the S/180 and M/155 ASDs was assessed to investigate the impact of crystallinity on polymer release profiles (Fig. 5). At 30 μg/mL BCL dose condition, corresponding to 70 μg/mL PVPVA, the release of PVPVA from the M/155 ASD (3.5% crystallinity) was rapid and nearly complete within 20 min. The concentration of PVPVA was ~63 μg/mL (corresponding to ~90% of the total PVPVA dose) within 20 min, and a plateau was observed over the subsequent 40 min. PVPVA dissolution from the crystal-free ASD powder (S/180) was initially rapid, but decelerated after 15 min, reaching ~60 μg/mL by 60 min. It is also interesting to note that the amount of PVPVA released from the crystal-free ASD powder was somewhat lower than that released from the M/155 ASD powder, with the difference decreasing at longer time points. The generally rapid and near-complete release of PVPVA from both samples is in contrast with what was observed for BCL dissolution (Fig. 2c) where only ~30–60% of the total BCL dose was released over 4 h. This observation is indicative of incongruent release behavior, with the polymer releasing faster than the drug (see Fig. S19) (10, 11).

DISCUSSION

Detection of Crystallinity in ASDs

Crystallinity is an important critical quality attribute (CQA) of ASD formulations. Ideally, a manufacturing process generates a fully amorphous system (47, 71). However, variability of the input raw materials or in the manufacturing process may result in a formulation with low levels of crystalline content. This crystallinity may or may not be a significant risk to formulation performance (23, 24). Ideally, specifications of input raw materials and the acceptable process design space would be established to limit this occurrence (47). In order to assess this risk, two technical issues must be addressed. First, low levels of crystallinity need to be detected (and quantified when possible). Second, the performance test needs to be well-designed to identify the crystallinity impact. This enables an assessment of the level of scrutiny required when selecting characterization techniques, designing methods, and setting specifications for crystalline content.

In this study, the HME process was designed to result in varying levels of residual crystallinity, and several analytical techniques were used to characterize the ASDs for crystallinity. TEM imaging detected crystallinity in three of the four formulations (Fig. 1e), while DSC, XRPD, SEM, and PLM found crystals in one or two of the formulations (Fig. 1a–d). This differential detectability between techniques prompts the question, when can a batch be declared amorphous? The common tool employed for crystallinity quantification, XRPD, has relatively low sensitivity to low levels of crystalline content (47, 61, 62), as observed herein. Although PLM has greater sensitivity, it cannot detect crystals sized below the diffraction limit; crystals within HME ASDs have been observed to be as small as 5–10 nm (24, 64, 66), and observed herein in the 100–500 nm size range (Fig. 1d, Fig. S13), and hence are undetectable by PLM. Due to the dynamic heating of a miscible drug-polymer system, DSC is not suitable for the detection of low levels of crystalline content where crystal dissolution can occur during the measurement (47, 61). To overcome these limitations, higher resolution analytical techniques must be employed to detect

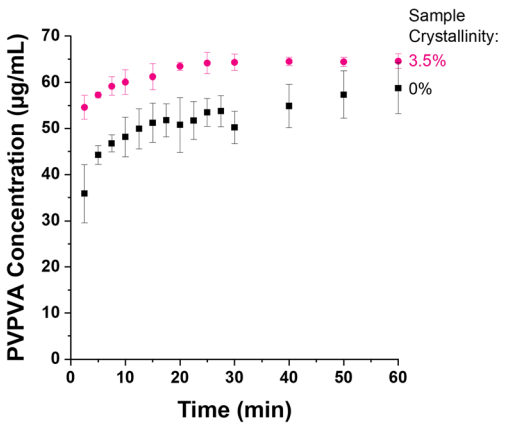

Fig. 5. PVPVA concentration *vs.* time from S/180 ASD (0% crystallinity) and M/155 ASDs (3.5% crystallinity) at the 30 μg/mL dose condition (corresponding to 70 μg/mL PVPVA dose). Error bar indicates one standard deviation (n=3)

low levels of crystallinity and/or samples containing very small crystals. Herein, TEM enabled the differentiation of two X-ray amorphous formulations (S/180 and S/155). Importantly, for this particular drug-polymer system, the results from performance testing subsequently showed clear evidence that the presence or absence of trace levels of crystallinity, detectable with TEM but not with the other methods, impacted both crystallization kinetics and outcomes in terms of the supersaturation profiles and polymorphic form (*vide infra*). These observations emphasize that the analytical methodology used to assess a CQA should be fit for purpose, i.e., able to detect the parameter of interest, in this case residual crystallinity, with the appropriate sensitivity.

Dissolution of BCL/PVPVA ASD Containing Residual Crystallinity

Varying Supersaturation Conditions

Competition between dissolution and crystallization from the BCL/PVPVA HME ASDs was found to be dependent on the dose concentration with higher supersaturation being observed for higher dose concentrations. Incomplete release of the amorphous BCL from the ASD system is observed for all formulations (with and without residual crystallinity). Due to effective nucleation and crystal growth inhibition by the polymer (Fig. S10), minimal crystallization via solution-mediated crystallization routes was observed. Thus, the solid-mediated crystallization (matrix) pathway appears to predominate for this ASD system, making residual crystallinity a key CQA impacting dissolution performance.

By observing the change in achievable supersaturation as the dose conditions are modulated (Fig. 6a), it is clear that matrix crystallization is the dominant mechanism taking place within the amorphous solid. Despite all dose conditions being at or below the amorphous solubility of 150 μg/mL (wherein all amorphous drug could theoretically dissolve in the absence of crystallization), the maximum achievable concentration was around 40 μg/mL. Higher doses enable greater achievable supersaturation before all amorphous solid is consumed by the growing crystals. This corresponds with the fraction dissolved reducing with each dose increase (Fig. 6b). In the absence of seed crystals, this indicates that the amount of amorphous solid correlates with the extent of crystallization, and provides support that the kinetics of matrix crystallization exceed those of dissolution in BCL/PVPVA ASDs. When seed crystals are added to the medium or are residual within the ASD solid, the fraction dissolved is reduced compared to the crystal-free ASD, as the crystals grow rapidly consuming any undissolved amorphous solid. However, even though the level of residual crystals varies from <1 to 30%, the overall achievable supersaturation is not easily correlated to the amount of seed crystals present (Fig. 6c), presumably because of the fast crystal growth rate of form 1 within the matrix when any level of seeds are present.

Because of the dominant role of matrix crystallization, different dissolution, supersaturation, and crystallization outcomes are observed for ASDs with and without residual crystallinity. The crystal-free BCL/PVPVA ASD (S/180, 0% crystallinity) shows "spring-and-parachute" dissolution behavior, schematically described in Fig. 7 a. Dissolution under non-sink conditions leads to a maximum concentration of ~40 μg/mL in about 1.5–2 h (Fig. 2). As seen from Fig. 5 and Fig. S19, the polymer releases faster than the drug, leading to enrichment of drug in the dissolving solid. With the substantial loss of polymer, the remaining undissolved, hydrated, amorphous drug-rich phase nucleates to polymorph form 2 crystals at the amorphous solid-liquid interfaces, initiating after about 20–30 min (as seen from Figs. 3 and 4). At this point, there are two competing processes occurring: (1) dissolution of remaining amorphous solid and (2) growth of form 2 crystals in close contact with amorphous solid. Eventually, all of the amorphous solid is consumed, either by dissolution, or by growth of the form 2 crystals, and the remaining polymer is expelled into solution. Some desupersaturation is observed at the highest non-sink conditions studied, which can be attributed to the higher amount of available solid added to the experiment and the overall higher supersaturation achieved; at higher supersaturation, PVPVA is less effective at delaying crystal growth (Fig. S10b). At the lower dose concentration (dose 30 μg/mL), the system has less solid surface area after matrix crystallization and the achieved supersaturation is lower; hence, no desupersaturation is observed. The concentration achieved is just above the form 2 polymorph apparent solubility of ~15 μg/mL. For all dose concentrations, complete release is never achieved because matrix crystallization occurs before all of the amorphous solid dissolves.

The dissolution and crystallization pathways of BCL/PVPVA ASDs containing residual crystals are schematically described in Fig. 7b. There are two major differences relative to the crystal-free system. First, reduced supersaturation levels are ultimately observed compared to the crystal-free ASD. Second, the crystallization outcome is different in terms of the polymorph that comprises the crystallized material. From PLM time-lapse imaging and Raman analysis, the residual crystals, which are the form 1 polymorph, are observed to grow, quickly consuming all available amorphous solid in under 1 h (Figs. 3–4). Hence, with the presence of form 1 crystals, even at trace levels of <1%, the growth of these crystals occurs much faster than the nucleation of the metastable form 2 polymorph. No significant desupersaturation is observed except at the highest supersaturation condition, again triggered by presence of greater levels of solid added to the experiment and higher maximum supersaturation achieved.

The matrix crystallization pathway in the presence of residual crystals is largely insensitive to the solution environment, as demonstrated by the observations made for the sink dissolution condition (Fig. 2d). The crystal-free ASD and crystalline physical mixture were able to achieve near-complete dissolution during the monitoring period. However, the dissolution profile of ASDs with residual crystallinity was reduced in comparison. This can be rationalized considering the local supersaturation of hydrated amorphous solid surrounding the form 1 residual crystals. This high local supersaturation favors crystal growth, as approximated by the crystal growth measurements performed at 150 μg/mL (Fig. S10b), in which extremely high crystal growth rates were observed in the absence of polymer in the buffer (and only moderately reduced by the presence of PVPVA). By growing crystals throughout the amorphous solid, the amount of

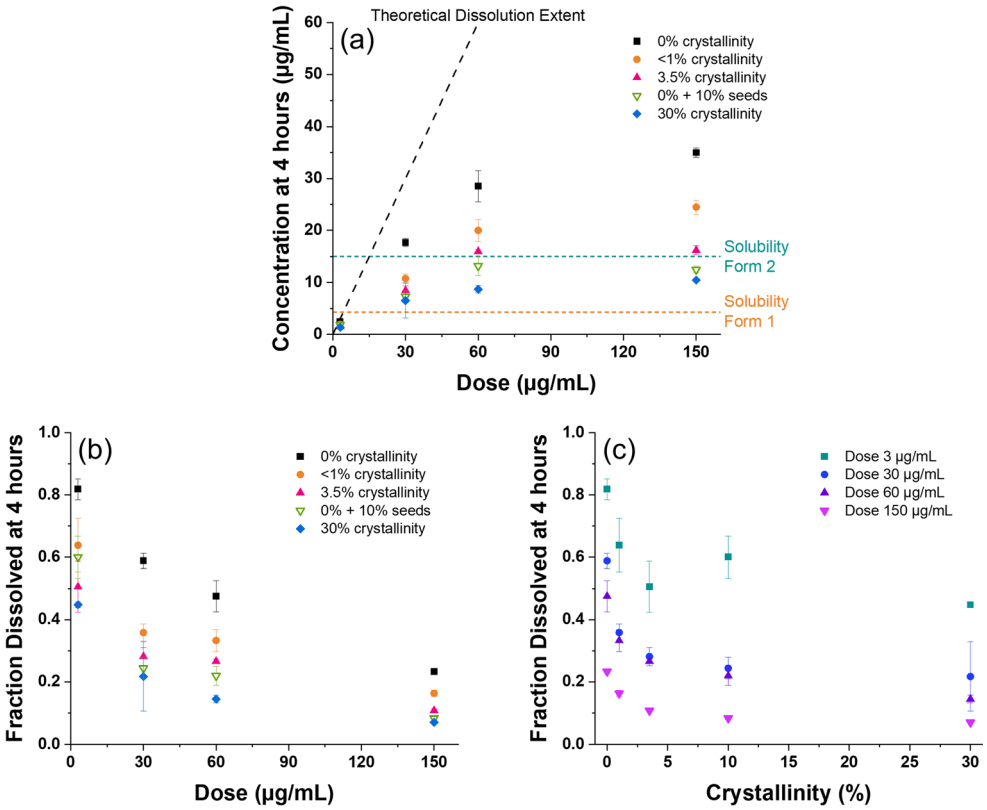

Fig. 6. **a** Comparison of the dose provided and concentration achieved at 4 h for samples with and without residual crystallinity. **b** Fraction dissolved at 4 h *vs.* dose provided. **c** Fraction dissolved at 4 h *vs.* % crystallinity. Error bar indicates one standard deviation (n=3)

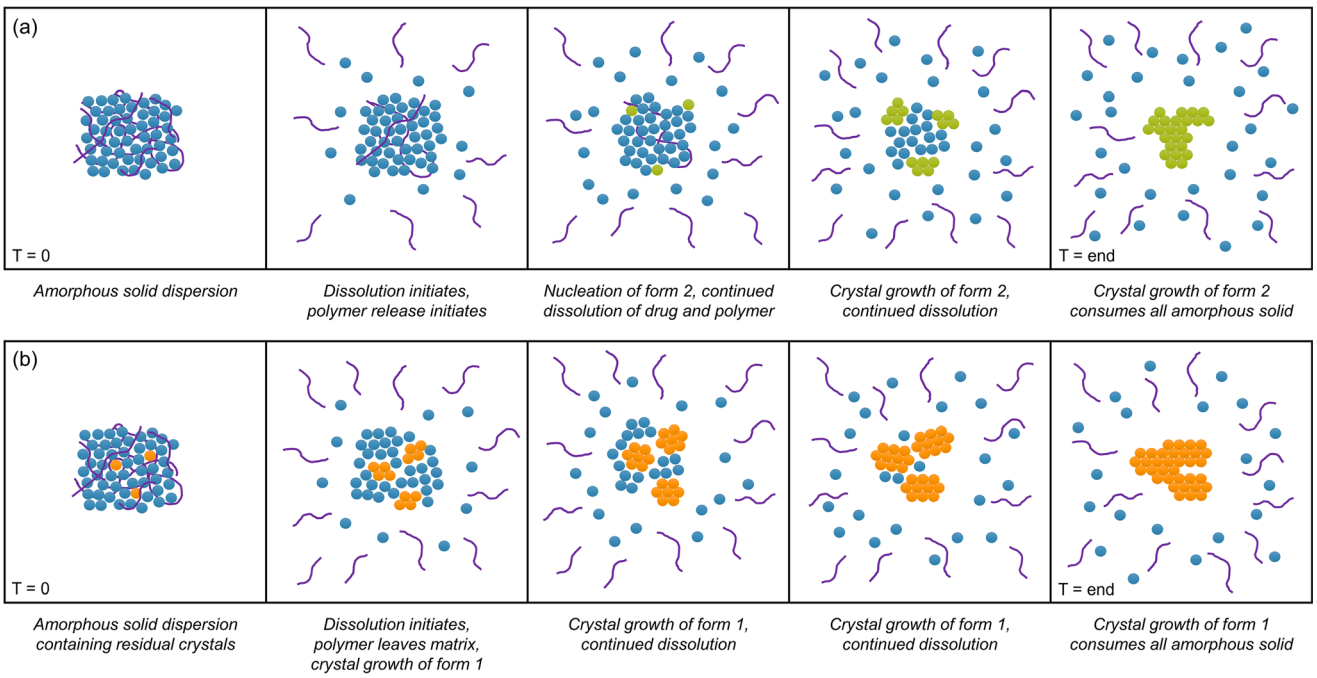

Fig. 7. Schematic of dissolution and crystallization pathways observed for BCL/PVPVA ASDs **a** without residual crystallinity and **b** with residual crystallinity. For a crystal-free amorphous solid, nucleation of the metastable polymorph (form 2, green) initiates at the interfaces of the amorphous solid-liquid boundary, then continues to grow consuming the amorphous solid. For an amorphous solid with residual crystallinity, crystal growth and dissolution proceed concurrently, with growth of the stable polymorph (form 1, orange). Dissolution terminates when all amorphous solid has been consumed by the growing crystalline form.

amorphous material available for dissolution is reduced. Ultimately, slow dissolution rates and reduced concentrations were achieved, even when compared to the crystalline physical mixture.

The use of HPMCAS confirms the matrix crystallization pathway. Although HPMCAS was found to be a highly effective nucleation and crystal growth inhibitor of solution-mediated crystallization (Fig. S10), it was generally unsuccessful as an inhibitor of matrix crystallization. Hence, the underlying mechanisms responsible for matrix crystallization must be understood in order to mitigate this failure mode.

Matrix Crystallization Mechanism

Matrix crystallization is clearly observed to be the dominant crystallization pathway in BCL/PVPVA ASD formulations both with and without residual crystals. Observations of matrix crystallization stem primarily from imaging or Raman spectroscopy of crystals developed in or at the surface of an amorphous structure, and are briefly reviewed here. Raina *et al*. observed that neat amorphous nifedipine crystallized upon exposure to buffer or buffer containing polymeric additives whereby matrix crystallization was prevented when the drug was formulated as an ASD (18). Xie *et al*. observed that the onset of matrix crystallization of neat amorphous celecoxib was not affected by the presence of polymeric additives in the dissolution buffer; however, the additives did delay the crystal growth rate (19). Saboo *et al*. noted that, in the case of indomethacin methyl ester ASD formulated with PVPVA, crystallization occurred at the surface of the tablet compact upon hydration, likely due to the low T_g of the compound and high crystallization tendency (26). Savolainen *et al*. used Raman spectroscopy to study crystallization kinetics from amorphous compacts of slow and fast crystallizing drugs, and found that amorphous indomethacin experienced matrix crystallization at the surface to the metastable α polymorph, whereas amorphous carbamazepine surfaces crystallized immediately upon contact with the dissolution medium (27). Clearly, the crystallization tendency of the amorphous, hydrated drug and (lack of) persistent intermolecular interactions between drug and polymer which serve to impede molecular reorganization likely play a role in the dominance of matrix crystallization.

In the amorphous BCL/PVPVA system, the amorphous solid gains significant molecular mobility upon hydration enabling it to crystallize. Preferential dissolution of PVPVA was observed (Fig. 5 and Fig. S19), as would be expected at such a high drug loading (10, 11, 26). The polymer rapidly depleted from the amorphous solid, changing the PVPVA:BCL solid ratio from 7:3 to 1:1 within 5 min. The rapid loss of the majority of the polymer leaves a hydrated, drug-rich amorphous solid, which likely has a T_g that is depressed below the temperature of the dissolution experiment (37°C), transitioning it into a supercooled liquid state (72). The dry T_g of BCL is 53°C and several percent (%) moisture uptake would be expected (73), significantly reducing the T_g of the hydrated amorphous material. (The wet T_g of the amorphous drug was unable to be measured due to the rapid crystallization of the neat amorphous form upon exposure to moisture.) This mobility enables the amorphous drug molecules to reorganize into a crystalline state to reduce their free energy, or integrate into nearby crystals (if present). Further, due to rapid polymer depletion, any drug-polymer intermolecular interactions that may have stabilized the ASD under ambient conditions are therefore disrupted in the hydrated environment.

The polymer release was observed to be even faster in the presence of residual crystallinity, rapidly changing the PVPVA:BCL solid ratio from 7:3 to 1:2 within 5 min. Polymer release is likely faster due to the expulsion of polymer from the amorphous domains upon integration of drug molecules into the residual crystals, which begins immediately upon exposure to the dissolution media (no induction time). In the absence of crystallinity, polymer release proceeded until a drug-rich layer was formed (Fig. 5), which served to slow or prevent polymer from inside the matrix to continue releasing. This reduction in polymer release rates has been observed in incongruently releasing ASDs during intrinsic dissolution characterization (10, 26). Upon nucleation, polymer can again begin to release, as it is expelled from the matrix.

Matrix crystallization (in the absence of residual crystallinity) is thus a surface-driven reaction, triggered by both hydration and rapid depletion of polymer due to incongruent dissolution of the ASD components. Ultimately, BCL is thus susceptible to matrix crystallization due to its physiochemical properties (including low T_g), high crystallization tendency, the high drug loading in the ASD, and the rapid dissolution of the polymer, reducing the concentration of the crystallization inhibitor. Further, BCL is known to be mechanically activated through processing operations such as milling and compression (51, 74), although the relevance of this factor to the observations of this study is unknown, as the same basic processing method was used to prepare all ASD samples. In the absence of residual crystallinity, the metastable form 2 polymorph is formed, consistent with Ostwald's step rule (75). However, if the stable crystal form is already present, either as residual crystals embedded within the ASD or as external seeds, the stable form grows. Importantly, these polymorphs have quite different solubilities; hence, the polymorphic outcome is an important consideration when determining the residual supersaturation after crystallization.

Seed Properties

External seeds are often added in *in vitro* experiments to predict how residual crystals might impact ASD dissolution performance (40, 43, 76). However, as is well known from crystallization science, all seeds are not created equal in terms of their potential for crystal growth (45, 77–79). Herein, upon addition of external crystal seeds (form 1) to the crystal-free ASD, the dissolution profile of the ASD was similar to that of the systems with residual crystals. Although the crystals are not embedded within the amorphous matrix, they quickly interact with and consume the amorphous solid, as observed by PLM imaging (Fig. 3). No nucleation and growth event of form 2 crystals is observed, due to the fast crystal growth of the form 1 seeds.

Notable differences in seed impact were readily apparent through analysis of the Raman crystallization profiles (Fig. 4).

Despite the greater level of external seeds added to the system (10% on a weight basis) than the two systems with residual crystals (<1% or 3.5%), the relative crystal growth rate was slower. This can be rationalized by considering the overall surface area of the crystal seeds rather than the level on a weight basis, as well as that the 10% seeds were external to the amorphous solid and had a different processing history. Based on relative crystallization rate, the total effective surface area for crystal growth of the systems can be rank ordered as S/180 (0% crystallinity) plus 10% seeds < S/155 (<1% crystallinity) < M/155 (3.5% crystallinity). This increased apparent crystallization potency follows from the size (surface area), location, and potential defectiveness of the residual crystals. The residual crystals are in the nanometer size range (Fig. 1d, Fig. S13), at least an order of magnitude smaller than the external seeds (which had a D_{50} particle size of 3.5 μm). Additionally, their internal location causes them to be more potent because they are embedded within the amorphous solid. Finally, previous studies have demonstrated that residual crystals in HME processed material can be highly defective, which may also contribute to a more rapid overall growth rate (24, 64, 67).

In the sink condition study, the residual crystals still triggered crystallization within the matrix, even though the bulk supersaturation was <1. The small residual crystals of initially high relative surface area grew rapidly into an agglomerated polycrystalline mass of low relative surface area. Because the concentrations were below the crystalline solubility, these crystals could continue dissolving, albeit more slowly than even the crystalline physical mixture. A similar phenomenon was likely observed by Wilson *et al.* whereby a crystalline physical mixture of enzalutamide/polymer outperformed a crystallized ASD in both *in vitro* and *in vivo* conditions (15). This observation highlights that it is critical to not only understand the crystallization kinetics of amorphous products, but to also characterize the properties of the resultant particulates. Small particles (under 1 μm) have traditionally been considered low risk to supersaturation, because of their increased solubility and dissolution rate (24, 40, 80). This is clearly not necessarily true for a matrix crystallization route, where the close proximity of the nanometer-sized crystals confined within the solid or external seeds interacting with amorphous solid surfaces will promote agglomeration to a low surface area polycrystalline material.

Risk Assessment

Two scenarios were described in our previous publication to describe the dissolution risk of ASD systems containing residual crystallinity (24). The low-risk scenario is defined by low crystal growth attributes, such as was found for indomethacin/PVPVA ASDs. In that system, due to extensive polymer adsorption to indomethacin crystals, crystal growth rates were near zero and hence residual crystallinity had little impact on dissolution performance. The high-risk scenario is defined by reduced rate and/or extent of dissolution compared to the crystal-free counterpart. For the BCL/PVPVA system, the fast crystal growth via matrix crystallization falls under this high-risk scenario. By fast amorphous-to-crystalline solid-state transformation, the amorphous solid was consumed faster than dissolution could proceed, limiting the extent of release and the supersaturation achieved. This was true even for crystallinity levels that were undetectable by XRPD.

For the two X-ray amorphous ASDs, the supersaturation achieved diverged due to differences in the underlying crystallization pathways for each sample. The crystal-free ASD S/180 nucleated the metastable polymorph (form 2), which has much higher solubility than form 1 (stable polymorph). In the S/155 ASD, containing initially trace levels of form 1 residual crystals, crystal growth proceeded rapidly and the available amorphous solid was consumed, which prevented higher levels of supersaturation. This pathway was consistently achieved, whether the form 1 crystal seeds were externally added or residual, interfering with the natural crystallization pathway of the amorphous solid to the metastable polymorph (form 2).

This study thus identifies a number of risk factors regarding presence of residual crystallinity on dissolution performance of an ASD.

(1) Solid-mediated (matrix) crystallization: When crystallization takes place directly through the solid matrix, the amorphous drug is prevented from dissolving to create a supersaturated solution. Of all crystallization routes, this pathway is the most critically detrimental to the formulation strategy, as the solubility advantage is never, or only moderately, realized. The crystal-free BCL/PVPVA ASD underwent matrix crystallization after an induction time, which enabled some supersaturation to be attained. External polymeric additives were largely ineffective in changing outcomes, offering at best a slight delay in nuclei formation in the matrix. Samples with residual crystallinity underwent matrix crystallization with no induction time. The amount of amorphous drug that could dissolve was limited by the amount of residual crystallinity (surface area) and the crystal growth rate.
(2) Solution-mediated crystallization: By inhibiting crystal growth from solution, polymers can be effective at reducing crystallization risk. This was notably observed in the indomethacin/PVPVA system, where extensive polymer adsorption inhibited crystal growth (24). Effective polymeric precipitation inhibition properties were also observed in this study, where PVPVA (and HPMCAS) exhibited nucleation and crystal growth inhibition of BCL (Fig. S10). However, the propensity of the BCL/PVPVA system to crystallize through the matrix route limited the impact of the effective solution-mediated polymeric precipitation inhibition.
(3) Seed properties: Properties of the seed crystals impact their ability to grow and consume supersaturation. Residual crystal seeds, being mechanically damaged and of small particle size/high relative surface area, are commonly more potent than bulk seeds (24, 45). Additionally, the residual crystals are embedded within an amorphous matrix, providing proximity for rapid integration of drug molecules, which are present at a high local supersaturation, into the crystal lattice.

(4) Polymorphic form: Crystallizing to the metastable polymorphic form is preferable. First, the metastable form has higher transient solubility, which enables a supersaturated solution to be maintained at that concentration (until a polymorphic transformation occurs). Second, slower solution-mediated crystal growth may be anticipated because the driving force is reduced. Thus, the presence of crystal seeds of the stable polymorphic form is highly detrimental, because the driving force for desupersaturation is greater.
(5) Supersaturation conditions: Modulating dose conditions can alter the balance of dissolution and crystallization pathways. Under higher dose conditions, more amorphous material is available to create supersaturation, which in turn leads to higher solution-mediated crystal growth rates. The apparent potency of crystal seeds at consuming supersaturation would be greatest under this scenario, which translates to a low fluid volume scenario. Matrix crystallization occurred irrespective of dose conditions.

CONCLUSION

Amorphous BCL, when formulated as an ASD with PVPVA, was found to be relatively robust against solution-mediated nucleation or crystal growth. However, in the presence of crystal seeds (stable polymorph form 1), both residual from the HME manufacturing process or externally added, the supersaturation achieved declined significantly. This was found to be due to the fast amorphous-to-crystalline transformation of the amorphous solid (matrix crystallization). Without crystal seeds, the metastable polymorph (form 2) nucleates at the solid interfaces during the dissolution experiment. In the presence of crystal seeds of the stable polymorph (form 1), this pathway is eliminated due to the crystal growth of form 1. Matrix crystallization is considered to be the most detrimental crystallization route for an amorphous formulation; thus, residual crystallinity (even trace levels) is of high risk to the performance of a BCL/PVPVA ASD. This study has implications for dissolution performance outcomes of ASDs containing crystallinity.

SUPPLEMENTARY INFORMATION

The online version contains supplementary material available at https://doi.org/10.1208/s12248-021-00598-6.

ACKNOWLEDGEMENTS

The authors thank Daniel DeNeve for the assistance with BET analysis and Clara Correa-Soto for the assistance with amorphous solubility measurement techniques.

AUTHOR CONTRIBUTION

Dana E. Moseson: conceptualization; methodology; investigation; writing—original draft; project administration; data curation; formal analysis; visualization

Isaac D. Corum: investigation; writing—review and editing

Andres Lust: methodology; investigation; writing—review and editing

Kevin J. Altman: investigation; writing—review and editing

Tze Ning Hiew: methodology, investigation; writing—review and editing

Ayse Eren: methodology; investigation; writing—review and editing

Zoltan K. Nagy: writing—review and editing; supervision

Lynne S. Taylor: conceptualization; writing—review and editing; supervision; funding acquisition

FUNDING

The authors gratefully acknowledge the financial support from the Dane O. Kildsig Center for Pharmaceutical Processing Research. The National Science Foundation Graduate Research Fellowship program is acknowledged for the financial support to D.M. under grant award DGE-1333468. The Mark and Kandy Fitch Fellowship is gratefully acknowledged for financial support to I.C.

DECLARATIONS

Conflict of Interest The authors declare no competing interests.

Disclaimer Any opinions, findings, and conclusions or recommendations expressed in this material are those of the author(s) and do not necessarily reflect the views of the National Science Foundation.

REFERENCES

1. McKelvey CA, Kesisoglou F. Enabling an HCV treatment revolution and the frontiers of solid solution formulation. J Pharm Sci. 2019;108-50–7.
2. Baghel S, Cathcart H, O'Reilly NJ. Polymeric amorphous solid dispersions: a review of amorphization, crystallization, stabilization, solid-state characterization, and aqueous solubilization of biopharmaceutical classification system class II drugs. J Pharm Sci. 2016;105:2527–44.
3. Schittny A, Huwyler J, Puchkov M. Mechanisms of increased bioavailability through amorphous solid dispersions: a review. Drug Deliv. 2020;27:110–27.
4. Alonzo DE, Gao Y, Zhou D, Mo H, Zhang GGZ, Taylor LS. Dissolution and precipitation behavior of amorphous solid dispersions. J Pharm Sci. 2011;100:3316–31.
5. Ilevbare GA, Taylor LS. Liquid-liquid phase separation in highly supersaturated aqueous solutions of poorly water-soluble drugs: implications for solubility enhancing formulations. Cryst Growth Des. 2013;13:1497–509.
6. Raina SA, Zhang GGZ, Alonzo DE, Wu J, Zhu D, Catron ND, et al. Enhancements and limits in drug membrane transport using supersaturated solutions of poorly water soluble drugs. J Pharm Sci. 2014;103:2736–48.
7. Sun DD, Lee PI. Evolution of supersaturation of amorphous pharmaceuticals: nonlinear rate of supersaturation generation regulated by matrix diffusion. Mol Pharm. 2015;12:1203–15.
8. Han YR, Ma Y, Lee PI. Impact of phase separation morphology on release mechanism of amorphous solid dispersions. Eur J Pharm Sci. 2019;136:104955.

9. Ueda K, Higashi K, Yamamoto K, Moribe K. Inhibitory effect of hydroxypropyl methylcellulose acetate succinate on drug recrystallization from a supersaturated solution assessed using nuclear magnetic resonance measurements. Mol Pharm. 2013;10:3801–11.
10. Saboo S, Mugheirbi NA, Zemlyanov DY, Kestur US, Taylor LS. Congruent release of drug and polymer: a "sweet spot" in the dissolution of amorphous solid dispersions. J Control Release. 2019;298:68–82.
11. Saboo S, Moseson DE, Szeto R, Kestur US, Taylor LS. Patterns of drug release as a function of drug loading from amorphous solid dispersions: a comparison of five different polymers. Eur J Pharm Sci. 2020;155:105514.
12. Bhugra C, Pikal MJ. Role of thermodynamic, molecular, and kinetic factors in crystallization from the amorphous state. J Pharm Sci. 2008;97:1329–49.
13. Kawakami K. Expert opinion on drug delivery supersaturation and crystallization : non- equilibrium dynamics of amorphous solid dispersions for oral drug delivery. Expert Opin Drug Deliv. 2017;14:735–43.
14. Rathi S, Chavan RB, Shastri NR. Classification of the crystallization tendency of active pharmaceutical ingredients (APIs) and nutraceuticals based on their nucleation and crystal growth behaviour in solution state. Drug Deliv Transl Res. 2020;10:70-82.
15. Wilson V, Lou X, Osterling DJ, Stolarik DF, Jenkins G, Gao W, et al. Relationship between amorphous solid dispersion in vivo absorption and in vitro dissolution: phase behavior during dissolution, speciation, and membrane mass transport. J Control Release. 2018;292:172–82.
16. Taylor LS, Zhang GGZ. Physical chemistry of supersaturated solutions and implications for oral absorption. Adv Drug Deliv Rev. 2016;101:122–42.
17. Alonzo DE, Zhang GGZ, Zhou D, Gao Y, Taylor LS. Understanding the behavior of amorphous pharmaceutical systems during dissolution. Pharm Res. 2010;27:608–18.
18. Raina SA, Alonzo DE, Zhang GGZ, Gao Y, Taylor LS. Impact of polymers on the crystallization and phase transition kinetics of amorphous nifedipine during dissolution in aqueous media. Mol Pharm. 2014;11:3565–76.
19. Xie T, Taylor LS. Dissolution performance of high drug loading celecoxib amorphous solid dispersions formulated with polymer combinations. Pharm Res. 2016;33:739–50.
20. Van Eerdenbrugh B, Raina SA, Hsieh Y-L, Augustijns P, Taylor LS. Classification of the crystallization behavior of amorphous active pharmaceutical ingredients in aqueous environments. Pharm Res. 2014;31:969–82.
21. Alonzo DE, Raina SA, Zhou D, Gao Y, Zhang GGZ, Taylor LS. Characterizing the impact of hydroxypropylmethyl cellulose on the growth and nucleation kinetics of felodipine from supersaturated solutions. Cryst Growth Des. 2012;12:1538–47.
22. Lin X, Hu Y, Liu L, Su L, Li N, Yu J, et al. Physical stability of amorphous solid dispersions: a physicochemical perspective with thermodynamic, kinetic and environmental aspects. Pharm Res. 2018;35:125.
23. Sun DD, Wen H, Taylor LS. Non-sink dissolution conditions for predicting product quality and in vivo performance of supersaturating drug delivery systems. J Pharm Sci. 2016;105:2477–88.
24. Moseson DE, Parker AS, Beaudoin SP, Taylor LS. Amorphous solid dispersions containing residual crystallinity: influence of seed properties and polymer adsorption on dissolution performance. Eur J Pharm Sci. 2020;146:105276.
25. Hancock BC, Parks M. What is the true solubility advantage for amorphous pharmaceuticals? Pharm Res. 2000;17:397–404.
26. Saboo S, Kestur US, Flaherty DP, Taylor LS. Congruent release of drug and polymer from amorphous solid dispersions: insights into the role of drug-polymer hydrogen bonding, surface crystallization and glass transition. Mol Pharm. 2020;17:1261–75.
27. Savolainen M, Kogermann K, Heinz A, Aaltonen J, Peltonen L, Strachan C, et al. Better understanding of dissolution behaviour of amorphous drugs by in situ solid-state analysis using Raman spectroscopy. Eur J Pharm Biopharm. 2009;71:71–9.
28. Grady H, Elder D, Webster GK, Mao Y, Lin Y, Flanagan T, et al. Industry's view on using quality control, biorelevant, and clinically relevant dissolution tests for pharmaceutical development, registration, and commercialization. J Pharm Sci. 2018;107:34–41.
29. Gray VA. Power of the dissolution test in distinguishing a change in dosage form critical quality attributes. AAPS PharmSciTech. 2018;19:3328–32.
30. Gray V, Kelly G, Xia M, Butler C, Thomas S, Mayock S. The science of USP 1 and 2 dissolution: present challenges and future relevance. Pharm Res. 2009;26:1289–302.
31. Sironi D, Bauer-Brandl A, Brandl M, Rosenberg J, Fricker G. The influence of liquid intake on the performance of an amorphous solid dispersion in rats. Eur J Pharm Biopharm. 2020;152:296–8.
32. Knopp MM, Chourak N, Khan F, Wendelboe J, Langguth P, Rades T, et al. Effect of polymer type and drug dose on the in vitro and in vivo behavior of amorphous solid dispersions. Eur J Pharm Biopharm. 2016;105:106–14.
33. Reppas C, Friedel HD, Barker AR, Buhse LF, Cecil TL, Keitel S, et al. Biorelevant in vitro performance testing of orally administered dosage forms - workshop report. Pharm Res. 2014;31:1867–76.
34. Trasi NS, Purohit HS, Taylor LS. Evaluation of the crystallization tendency of commercially available amorphous tacrolimus formulations exposed to different stress conditions. Pharm Res. 2017:1–14.
35. Purohit HS, Trasi NS, Sun DD, Chow ECY, Wen H, Zhang X, et al. Investigating the impact of drug crystallinity in amorphous tacrolimus capsules on pharmacokinetics and bioequivalence using discriminatory in vitro dissolution testing and physiologically based pharmacokinetic modeling and simulation. J Pharm Sci. 2018;107:1330–41.
36. Purohit HS, Trasi NS, Osterling DJ, Stolarik DF, Jenkins GJ, Gao W, et al. Assessing the impact of endogenously derived crystalline drug on the in vivo performance of amorphous formulations. Mol Pharm. 2019;16:3617–25.
37. Hate S, Reutzel-Edens SM, Taylor LS. Absorptive dissolution testing: an improved approach to study the impact of residual crystallinity on the performance of amorphous formulations. J Pharm Sci. 2020;109:1312–23.
38. Priemel PA, Grohganz H, Gordon KC, Rades T, Strachan CJ. The impact of surface- and nano-crystallisation on the detected amorphous content and the dissolution behaviour of amorphous indomethacin. Eur J Pharm Biopharm. 2012;82:187–93.
39. Mah PT, Laaksonen T, Rades T, Peltonen L, Strachan CJ. Differential scanning calorimetry predicts the critical quality attributes of amorphous glibenclamide. Eur J Pharm Sci. 2015;80:74–81.
40. Hermans A, Kesisoglou F, Xu W, Dewitt K, Marota M, Colace T. Possibilities and limiting factors for use of dissolution as a quality control tool to detect presence of crystallinity for amorphous solid dispersions: an experimental and modeling investigation. J Pharm Sci. 2019;108:3054–62.
41. Greco K, Bogner R. Crystallization of amorphous indomethacin during dissolution: effect of processing and annealing. Mol Pharm. 2010;7:1406–18.
42. Li N, Cape JL, Mankani BR, Zemlyanov DY, Shepard KB, Morgen MM, et al. Water-induced phase separation of spray-dried amorphous solid dispersions. Mol Pharm. 2020;17:4004–17.
43. Knopp MM, Wendelboe J, Holm R, Rades T. Effect of amorphous phase separation and crystallization on the in vitro and in vivo performance of an amorphous solid dispersion. Eur J Pharm Biopharm. 2018;130:290–5.
44. Ricarte RG, Zee NJ Van, Li Z, Johnson LM, Lodge TP, Hillmyer MA. Recent advances in understanding the micro- and nanoscale phenomena of amorphous solid dispersions. Mol Pharm. 2019;16:4089–103.
45. Que C, Gao Y, Raina SA, Zhang GGZ, Taylor LS. Paclitaxel crystal seeds with different intrinsic properties and their impact on dissolution of paclitaxel-HPMCAS amorphous solid dispersions. Cryst Growth Des. 2018;18:1548–59.

46. Ojo AT, Ma C, Lee PI. Elucidating the effect of crystallization on drug release from amorphous solid dispersions in soluble and insoluble carriers. Int J Pharm. 2020;591:120005.
47. Moseson DE, Taylor LS. The application of temperature-composition phase diagrams for hot melt extrusion processing of amorphous solid dispersions to prevent residual crystallinity. Int J Pharm. 2018;553:454–66.
48. Evans RC, Bochmann ES, Kyerematen SO, Wagner KG. Holistic QbD approach for hot-melt extrusion process design space evaluation: linking materials science, experimentation and process modeling. Eur J Pharm Biopharm. 2019;141;149–60.
49. Abu Bakar MR, Nagy ZK, Saleemi AN, Rielly CD. The impact of direct nucleation control on crystal size distribution in pharmaceutical crystallization processes. Cryst Growth Des. 2009;9:1378–84.
50. Vega DR, Polla G, Martinez A, Mendioroz E, Reinoso M. Conformational polymorphism in bicalutamide. Int J Pharm. 2007;328:112–8.
51. Nemet Z, Sztatisz J, Demeter A. Polymorph transitions of bicalutamide: a remarkable example of mechanical activation. J Pharm Sci. 2008;97:3222–32.
52. Almeida E, Sousa L, Reutzel-Edens SM, Stephenson GA, Taylor LS. Assessment of the amorphous "solubility" of a group of diverse drugs using new experimental and theoretical approaches. Mol Pharm. 2015;12:484–95.
53. Raina SA, Alonzo DE, Zhang GGZ, Gao Y, Taylor LS. Using environment-sensitive fluorescent probes to characterize liquid-liquid phase separation in supersaturated solutions of poorly water soluble compounds. Pharm Res. 2015;32:3660–73.
54. Schram CJ, Taylor LS, Beaudoin SP. Influence of polymers on the crystal growth rate of felodipine: correlating adsorbed polymer surface coverage to solution crystal growth inhibition. Langmuir. 2015;31:11279–87.
55. LaFountaine JS, McGinity JW, Williams RO. Challenges and strategies in thermal processing of amorphous solid dispersions: a review. AAPS PharmSciTech. 2016;17:43–55.
56. Gupta SS, Meena AK, Parikh T, Serajuddin ATM. Investigation of thermal and viscoelastic properties of polymers relevant to hot melt extrusion - I: polyvinylpyrrolidone and related polymers. J Excipients Food Chem. 2014;5:32–45.
57. Tres F, Coombes SR, Phillips AR, Hughes LP, Wren SAC, Aylott JW, et al. Investigating the dissolution performance of amorphous solid dispersions using magnetic resonance imaging and proton NMR. Molecules. 2015;20:16404–18.
58. Tres F, Patient JD, Williams PM, Treacher K, Booth J, Hughes LP, et al. Monitoring the dissolution mechanisms of amorphous bicalutamide solid dispersions via real-time Raman mapping. Mol Pharm. 2015;12:1512–22.
59. Szafraniec J, Antosik A, Knapik-Kowalczuk J, Gawlak K, Kurek M, Szlęk J, et al. Molecular disorder of bicalutamide—amorphous solid dispersions obtained by solvent methods. Pharmaceutics. 2018;10:194.
60. Andrews GP, Abudiak OA, Jones DS. Physicochemical characterization of hot melt extruded bicalutamide-polyvinylpyrrolidone solid dispersions. J Pharm Sci. 2010;99:1322–35.
61. Dedroog S, Pas T, Vergauwen B, Huygens C, Mooter G Van den. Solid-state analysis of amorphous solid dispersions: why DSC and XRPD may not be regarded as stand-alone techniques. J Pharm Biomed Anal. 2019;178:112937.
62. Shah B, Kakumanu VK, Bansal AK. Analytical techniques for quantification of amorphous/crystalline phases in pharmaceutical solids. J Pharm Sci. 2006;95:1641–65.
63. Rumondor ACF, Taylor LS. Application of partial least-squares (PLS) modeling in quantifying drug crystallinity in amorphous solid dispersions. Int J Pharm. 2010;398:155–60.
64. Moseson DE, Mugheirbi NA, Stewart AA, Taylor LS. Nanometer-scale residual crystals in a hot melt extruded amorphous solid dispersion: characterization by transmission electron microscopy. Cryst Growth Des. 2018;18:7633–40.
65. Haser A, Cao T, Lubach J, Listro T, Acquarulo L, Zhang F. Melt extrusion vs. spray drying: the effect of processing methods on crystalline content of naproxen-povidone formulations. Eur J Pharm Sci. 2017;102:115–25.
66. S'ari M, Blade H, Cosgrove S, Drummon-Brydson R, Hondow N, Hughes LP, et al. Characterization of amorphous solid dispersions and identification of low levels of crystallinity by transmission electron microscopy. Mol Pharm. 2021;18:1905–19.
67. Moseson DE, Parker AS, Gilpin CJ, Stewart AA, Beaudoin SP, Taylor LS. Dissolution of indomethacin crystals into a polymer melt: role of diffusion and fragmentation. Cryst Growth Des. 2019;19:3315–28.
68. Elkhabaz A, Moseson DE, Sarkar S, Brouwers J, Simpson GJ, Augustijns P, et al. Crystallization kinetics in fasted-state simulated and aspirated human intestinal fluids. Cryst Growth Des. 2021. https://doi.org/10.1021/acs.cgd.0c01730
69. Michaels AS, Colville AR. The effect of surface active agents on crystal growth rate and crystal habit. J Phys Chem. 1960;64:13–19.
70. Takubo H, Kume S, Koizumi M. Relationships between supersaturation, solution velocity, crystal habit and growth rate in crystallization of $NH_4H_2PO_4$. J Cryst Growth. 1984;67:217–26.
71. Butreddy A, Bandari S, Repka MA. Quality-by-design in hot melt extrusion based amorphous solid dispersions: an industrial perspective on product development. Eur J Pharm Sci. 2020;105655.
72. Newman A, Zografi G. An examination of water vapor sorption by multicomponent crystalline and amorphous solids and its effects on their solid-state properties. J Pharm Sci. 2019;108:1061–80.
73. Murdande SB, Pikal MJ, Shanker RM, Bogner RH. Solubility advantage of amorphous pharmaceuticals: II. Application of quantitative thermodynamic relationships for prediction of solubility enhancement in structurally diverse insoluble pharmaceuticals. Pharm Res. 2010;27:2704–14.
74. Szafraniec-Szczęsny J, Antosik-Rogóż A, Knapik-Kowalczuk J, Kurek M, Szefer E, Gawlak K, et al. Compression-induced phase transitions of bicalutamide. Pharmaceutics. 2020;12:438.
75. Byrn SR, Zografi G, Chen X (Sean). Polymorphs. In: Solid State Properties of Pharmaceutical Materials. New York: John Wiley & Sons; 2017. p. 22–37.
76. Koyama H, Ito M, Terada K, Sugano K. Effect of seed particles on precipitation of weak base drugs in physiological intestinal conditions. Mol Pharm. 2016;13:2711–7.
77. Mullin JW. Crystal growth. In: Crystallization. Boston: Oxford; 2001. p. 216–88.
78. Aamir E, Nagy ZK, Rielly CD. Evaluation of the effect of seed preparation method on the product crystal size distribution for batch cooling crystallization processes. Cryst Growth Des. 2010;10:4728–40.
79. Frawley PJ, Mitchell NA, Ó'Ciardhá CT, Hutton KW. The effects of supersaturation, temperature, agitation and seed surface area on the secondary nucleation of paracetamol in ethanol solutions. Chem Eng Sci. 2012;75:183–97.
80. Jermain SV, Brough C, Williams RO. Amorphous solid dispersions and nanocrystal technologies for poorly water-soluble drug delivery – an update. Int J Pharm. 2018;535:379–92.